

# Voltage imaging and optogenetics reveal behaviour-dependent changes in hippocampal dynamics

Yoav Adam<sup>1</sup>, Jeong J. Kim<sup>1</sup>, Shan Lou<sup>1</sup>, Yongxin Zhao<sup>2</sup>, Michael E. Xie<sup>1</sup>, Daan Brinks<sup>1</sup>, Hao Wu<sup>1</sup>, Mohammed A. Mostajo-Radji<sup>3</sup>, Simon Kheifets<sup>1</sup>, Vicente Parot<sup>1</sup>, Selmaan Chettih<sup>4</sup>, Katherine J. Williams<sup>1</sup>, Benjamin Gmeiner<sup>1</sup>, Samouil L. Farhi<sup>1</sup>, Linda Madisen<sup>5</sup>, E. Kelly Buchanan<sup>6</sup>, Ian Kinsella<sup>6</sup>, Ding Zhou<sup>6</sup>, Liam Paninski<sup>6</sup>, Christopher D. Harvey<sup>4</sup>, Hongkui Zeng<sup>5</sup>, Paola Arlotta<sup>3</sup>, Robert E. Campbell<sup>2</sup> & Adam E. Cohen<sup>1,7\*</sup>

A technology that simultaneously records membrane potential from multiple neurons in behaving animals will have a transformative effect on neuroscience research<sup>1,2</sup>. Genetically encoded voltage indicators are a promising tool for these purposes; however, these have so far been limited to single-cell recordings with a marginal signal-to-noise ratio in vivo<sup>3–5</sup>. Here we developed improved near-infrared voltage indicators, high-speed microscopes and targeted gene expression schemes that enabled simultaneous in vivo recordings of supra- and subthreshold voltage dynamics in multiple neurons in the hippocampus of behaving mice. The reporters revealed subcellular details of back-propagating action potentials and correlations in subthreshold voltage between multiple cells. In combination with stimulation using optogenetics, the reporters revealed changes in neuronal excitability that were dependent

on the behavioural state, reflecting the interplay of excitatory and inhibitory synaptic inputs. These tools open the possibility for detailed explorations of network dynamics in the context of behaviour.

Archaeorhodopsin 3 (Arch)-derived genetically encoded voltage indicators (GEVIs) are excited by red light and emit in the near-infrared part of the spectrum, have sub-millisecond response times and report neuronal action potentials with an approximately 40% increase in fluorescence<sup>6</sup>. Expression of the Arch-based GEVI QuasAr2 and the channelrhodopsin (ChR) CheRiff (together called ‘Optopatch2’) in a transgenic mouse enabled optical stimulation and recording in sparsely expressing acute brain slices<sup>3</sup>, but did not attain an adequate signal-to-noise ratio (SNR) for voltage imaging in the brain in vivo owing to poor GEVI trafficking and high background fluorescence.

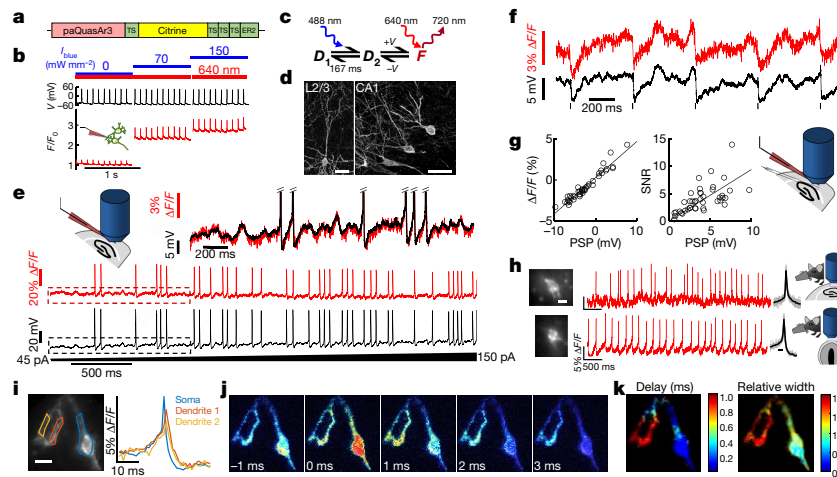


**Fig. 1 | Photoactivated QuasAr3 (paQuasAr3) reports neuronal activity in vivo.** **a**, Schematic of the paQuasAr3 construct. **b**, Photoactivation by blue light enhanced voltage signals excited by red light in cultured neurons that expressed paQuasAr3 (representative example of  $n = 4$  cells). **c**, Model of the photocycle of paQuasAr3. **d**, Confocal images of sparsely expressed paQuasAr3 in brain slices. Scale bars, 50  $\mu\text{m}$ . Representative images, experiments were repeated in  $n = 3$  mice. **e**, Simultaneous fluorescence and patch-clamp recordings from a neuron expressing paQuasAr3 in acute brain slice. Top, magnification of boxed regions. Schematic shows brain slice, patch pipette and microscope objective. **f**, Simultaneous fluorescence and patch-clamp recordings of inhibitory post synaptic potentials in an L2–3 neuron induced by electrical stimulation of L5–6 in acute slice. **g**, Normalized change in fluorescence ( $\Delta F/F$ ) and SNR of optically recorded post-synaptic potentials (PSPs) as a function of the amplitude of the post-synaptic potentials. The voltage sensitivity was  $\Delta F/F = 40 \pm 1.7\%$

per 100 mV. The SNR was  $0.93 \pm 0.07$  per 1 mV in a 1-kHz bandwidth ( $n = 42$  post-synaptic potentials from 5 cells, data are mean  $\pm$  s.d.). Schematic shows brain slice, patch pipette, field stimulation electrodes and microscope objective. **h**, Optical measurements of paQuasAr3 fluorescence in the CA1 region of the hippocampus (top) and glomerular layer of the olfactory bulb (bottom) of anaesthetized mice (representative traces from  $n = 7$  CA1 cells and  $n = 13$  olfactory bulb cells,  $n = 3$  mice). Schematics show microscope objective and the imaged brain region. **i**, STA fluorescence from 88 spikes in a CA1 oriens neuron. **j**, Frames from the STA video showing the delay in the back-propagating action potential in the dendrites relative to the soma. **k**, Sub-Nyquist fitting of the action potential delay and width shows electrical compartmentalization in the dendrites. Experiments in **k–m** were repeated in  $n = 2$  cells from  $n = 2$  mice.

<sup>1</sup>Department of Chemistry and Chemical Biology, Harvard University, Cambridge, MA, USA. <sup>2</sup>Department of Chemistry, University of Alberta, Edmonton, Alberta, Canada. <sup>3</sup>Department of Stem Cell and Regenerative Biology, Harvard University, Cambridge, MA, USA. <sup>4</sup>Department of Neurobiology, Harvard Medical School, Boston, MA, USA. <sup>5</sup>Allen Institute for Brain Science, Seattle, WA, USA. <sup>6</sup>Department of Statistics, Columbia University, New York, NY, USA. <sup>7</sup>Howard Hughes Medical Institute, Chevy Chase, MD, USA. \*e-mail: [cohen@chemistry.harvard.edu](mailto:cohen@chemistry.harvard.edu)

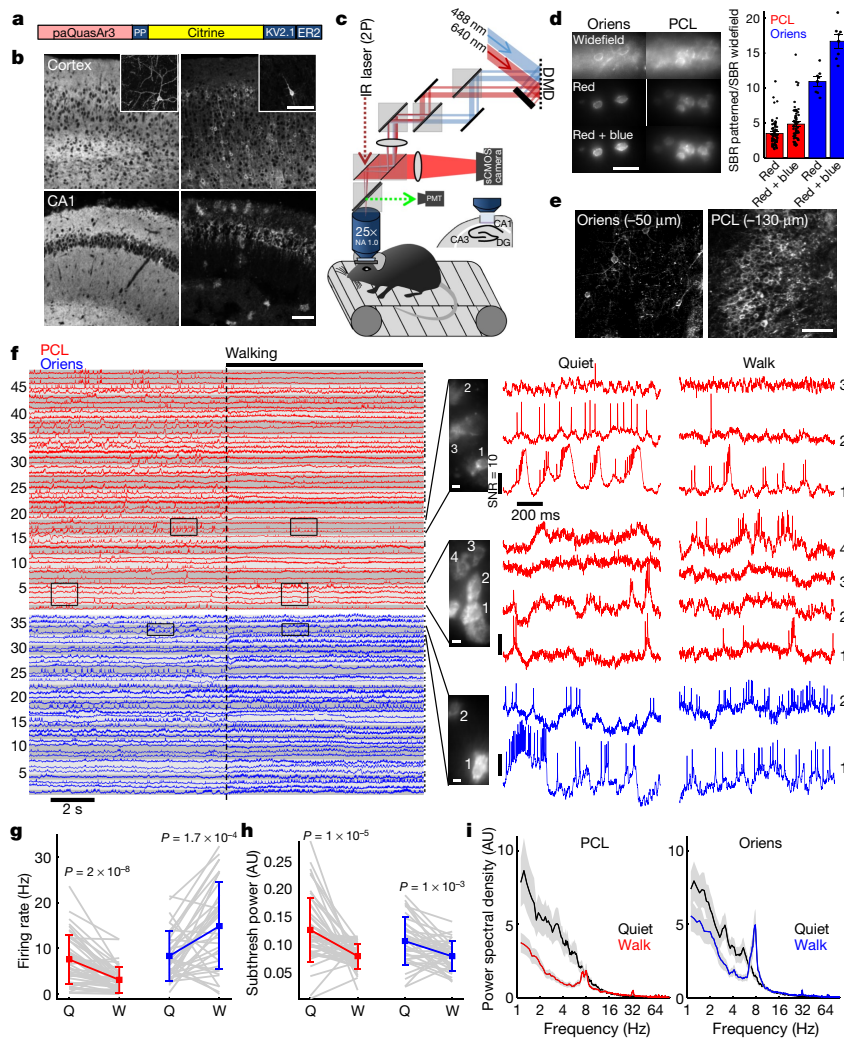


**Fig. 2 | Optical recording of neuronal activity in hippocampus of walking mice.** **a**, Schematic of the paQuasAr3-s construct. **b**, Confocal images of brain slices. Broadly expressed paQuasAr3 filled the neuropil, preventing optical resolution of individual cells (left), whereas paQuasAr3-s resolved cell bodies (right). Insets, sparsely expressed constructs show the difference in dendritic expression between paQuasAr3 and paQuasAr3-s. Scale bars, 100  $\mu\text{m}$ . Representative images, repeated in  $n = 2$  mice per condition. **c**, Optical system for simultaneous two-photon (2P) imaging and patterned illumination with red and blue light. DMD, digital micromirror device; IR, infrared; NA, numerical aperture. **d**, Left, epifluorescence images. Right, Quantification. Top, epifluorescence images with wide-field red illumination of paQuasAr3-s in the CA1 region of the hippocampus in vivo. Middle, same fields of view with patterned red illumination. Bottom, addition of patterned blue illumination increased the image contrast. Scale bar, 50  $\mu\text{m}$ . Right,

effect of patterned red and blue light on signal-to-background ratio (SBR) in the oriens and PCL (PCL,  $n = 64$  cells from  $n = 2$  mice; oriens,  $n = 7$  cells from  $n = 2$  mice; data are mean  $\pm$  s.e.m.). **e**, Two-photon fluorescence images of paQuasAr3-s expression in the oriens (left) and the PCL (right). Scale bar, 100  $\mu\text{m}$ . **f**, Fluorescence recordings from PCL (red) and oriens (blue,  $n = 5$  mice). Traces with similarly shaded backgrounds were acquired simultaneously. Right, magnified views show complex spikes, bursts, correlated activity between cells and modulation of the spiking by subthreshold dynamics. **g–i**, Effect of brain state (quiet or walking) on firing rate (**g**), total power in the subthreshold oscillations (**h**) and population-average power spectra (**i**) in the PCL (red) and the oriens (blue). AU, arbitrary units. **f–i**,  $n = 48$  cells in the PCL, 36 cells in oriens,  $n = 5$  mice. **g, h**, Data are mean  $\pm$  s.d., paired Student's  $t$ -test. **i**, Line and shading shows mean  $\pm$  s.e.m.

We rationally designed multiple constructs and tested them for the SNR of optogenetically induced action potentials in culture and in brain slices. This screen led to a construct, QuasAr3, that showed high expression and excellent trafficking in vivo and reported action potentials in acute slices with fast kinetics and a high SNR ( $21 \pm 12$  (mean  $\pm$  s.d.) in a 1-kHz bandwidth,  $n = 10$  neurons, Extended Data Fig. 1). We generated a transgenic mouse with Cre-dependent QuasAr3 and CheRiff in the highly expressing TIGRE locus<sup>7</sup>. Acute slices from these animals yielded a high SNR in genetically targeted all-optical electrophysiology recordings and clearly showed cell-type-specific differences in firing patterns (Extended Data Fig. 2).

We then tested a point mutation in QuasAr3 (V59A), the homologue of which causes photoswitching behaviour<sup>8</sup> in bacteriorhodopsin (V49A) and enhances the population of the fluorescent Q state<sup>9</sup>. Under continuous red excitation ( $\lambda_{\text{exc}} = 640$  nm,  $10$  W  $\text{mm}^{-2}$ ), illumination with moderate-intensity blue light ( $\lambda_{\text{act}} = 488$  nm,  $100$  mW  $\text{mm}^{-2}$ ) reversibly increased near-infrared fluorescence ( $\lambda_{\text{em}} = 660$ – $740$  nm) of QuasAr3(V59A) by a factor of  $2.9 \pm 0.7$  ( $n = 8$  cells; Extended Data Fig. 3). Blue light enhanced voltage-dependent fluorescence in HEK293T cells (Extended Data Fig. 3) and cultured neurons (Fig. 1b) by 2–3-fold. We called QuasAr3(V59A) ‘photoactivated QuasAr3’ (paQuasAr3). A detailed characterization of the kinetic, spectroscopic

and voltage-dependent properties of paQuasAr3 (Extended Data Fig. 3) led to the proposed photocycle model shown in Fig. 1c. Blue light transferred the population from a dark state,  $D_1$ , to a voltage-sensitive equilibrium between a second dark state,  $D_2$ , and a fluorescent state,  $F$ .

PaQuasAr3 expressed in vivo by viral transduction trafficked well in soma and dendrites (Fig. 1d). Recordings in acute cortical slices showed that photoactivation by blue light significantly improved the SNR for spike detection (Fig. 1e, Extended Data Fig. 3; QuasAr3, SNR =  $20 \pm 12$ ; paQuasAr3 red only, SNR =  $27 \pm 10$ ; paQuasAr3 red and blue, SNR =  $37 \pm 14$ ;  $n = 10$  cells in each group). PaQuasAr3 resolved 1–2 mV fluctuations, including subthreshold post-synaptic potentials (Fig. 1f, g).

The enhanced SNR from paQuasAr3 enabled single-neuron optical voltage measurements in the CA1 region of the hippocampus and in the glomerular layer of the olfactory bulb of anaesthetized mice (Fig. 1h). In a CA1 oriens interneuron that expressed paQuasAr3, we observed back-propagating action potentials in dendrites (Fig. 1i–k). A spike-triggered average (STA) video showed a conduction delay between the cell body and the nearby dendrites. Using a sub-Nyquist interpolation algorithm<sup>6</sup>, we observed electrical compartmentalization of the distal dendrites (Fig. 1i–k and Methods), as anticipated<sup>10</sup>.

To record from multiple neurons in densely expressing samples, we fused paQuasAr3 with a trafficking motif from the soma-localized  $Kv2.1$  potassium channel<sup>11,12</sup>, which led to largely soma-localized expression (Fig. 2a, b). We called this construct paQuasAr3-s. Patch-clamp recording in acute brain slices confirmed that expression of paQuasAr3-s and the other QuasAr3 constructs used in this study did not affect membrane electrical properties (Extended Data Fig. 3).

We performed optical recordings from the hippocampus, in the oriens layer (20–60  $\mu\text{m}$  below the hippocampal surface) and in the pyramidal cell layer (PCL, up to 130  $\mu\text{m}$  depth). To enhance the signal-to-background ratio in vivo, we developed a custom dual-wavelength micromirror-based illumination system to deliver both the red excitation and the blue sensitization light (Fig. 2c). The red illumination was patterned to impinge only on the cell bodies, avoiding the interstitial regions that contributed to background. Patterned red illumination (5–15 mW per cell in the PCL, 5–30 mW per cell in the oriens) enhanced the signal-to-background ratio by a factor of  $3.5 \pm 0.2$  in the PCL and  $11 \pm 1$  in the oriens (Fig. 2d and Extended Data Fig. 4). Adding patterned blue illumination, (10–60  $\mu\text{W}$  per cell), enhanced the signal-to-background ratio by an additional 40–50%, which led to a net improvement over wide-field illumination of  $4.9 \pm 0.3$  in the PCL and  $16.7 \pm 1.0$  in the oriens (Fig. 2d and Extended Data Fig. 4). Patterned red and blue illumination also substantially improved the SNR for spike detection (Extended Data Fig. 4).

To test for laser-induced heating or photodamage, we quantified the effect of the red illumination on the spontaneous firing rate of neurons. We observed no change in spontaneous firing rate with illumination of up to 80 mW into the tissue (spread over 10 pyramidal cells). Numerical simulations of laser-induced heating showed that for 100 mW in the tissue, brain temperature remained  $<37^\circ\text{C}$  (Extended Data Fig. 4). Optical recordings showed approximately 50% photobleaching during a 10-min recording (Extended Data Fig. 5), but reporter expression recovered within 1 week (Extended Data Fig. 8). High-quality recordings were obtained throughout times tested (three weeks to three months after viral gene delivery).

To investigate changes in activity that are dependent on the brain state, we recorded from awake, head-fixed mice that were walking on a motorized treadmill, during 10–15 s of rest, followed by 15 s of walking (Methods). Recordings were made from  $n = 5$  mice and included 48 spiking neurons in the PCL from 19 fields of view and 36 spiking neurons in the oriens from 20 fields of view (Fig. 2f). We adapted an activity-based segmentation method<sup>13</sup> to resolve single-neuron signals from densely expressing fields of view and validated the method using

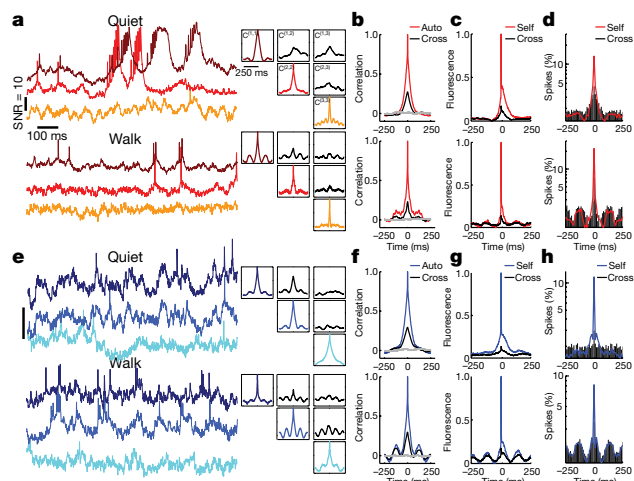


**Fig. 3 | Behaviour-dependent intercellular correlations in the hippocampus.** **a–d**, Data were obtained in the PCL. **e–h**, Data were obtained in the oriens. **a, e**, Left, samples of recordings from a trio of cells in the PCL (**a**) and oriens (**e**). Top, during quiet. Bottom, during walking. Representative traces of 19 fields of view in the PCL and 20 fields of view in the oriens. Right, auto- and cross-correlations of the fluorescence traces, calculated from 9-s recordings in each brain region and behavioural state. The auto- and cross-correlations clearly show an enhanced  $\theta$ -rhythm in both brain regions during walking and differing cross-correlations between simultaneously recorded pairs of cells. **b, f**, Grand average auto- and cross-correlations during quiet (top) and walking (bottom) in the PCL ( $n = 46$  cells for autocorrelations, 43 pairs for cross-correlations) and oriens ( $n = 29$  cells for autocorrelations, 19 pairs for cross-correlations). Grey line, mean cross-correlation between randomly selected cells from different fields of view. **c, g**, Spike-triggered grand average fluorescence during quiet (top) and walking (bottom) in the PCL ( $n = 86$  pairs) and oriens ( $n = 38$  pairs). During walking, spikes in both layers occurred on average on the rising edge of the STA  $\theta$ -rhythm, leading to a  $22^\circ$  phase shift in the PCL and  $42^\circ$  shift in the oriens between the mean spike and the peak of the mean intracellular  $\theta$ -rhythm. **d, h**, Spike-triggered grand average spiking probability during quiet (top) and walking (bottom) in the PCL (quiet,  $n = 4,796$  spikes; walking,  $n = 1,983$  spikes) and oriens (quiet,  $n = 2,719$  spikes; walking,  $n = 4,258$  spikes). The y axis is shown as a log scale.

extensive simulations, composite videos and patch-clamp recordings in acute slices (Extended Data Fig. 6 and Methods).

Typical recordings resolved 2–4 spiking cells simultaneously in the PCL and up to 3 spiking cells simultaneously in the oriens (Fig. 2f). In an anaesthetized animal, we recorded from up to seven spiking cells simultaneously (Extended Data Fig. 7). All fluorescence traces are displayed at the native 1-kHz recording bandwidth, without smoothing. Fluorescence traces clearly resolved hallmarks of intracellular activity in the CA1, including simple and complex spikes, bursts, subthreshold depolarizations and  $\theta$ -frequency oscillations<sup>14–17</sup> (Fig. 2f).

Forced walking decreased the mean spike rate of PCL neurons (from  $7.6 \pm 5.3$  Hz to  $3.1 \pm 2.8$  Hz) but, consistent with previous reports<sup>18</sup>, increased the mean spike rate of oriens neurons (from  $8.3 \pm 5.4$  Hz to  $14.9 \pm 9.5$  Hz; Fig. 2g). Walking decreased the overall power of the subthreshold oscillations in both the PCL (1.9  $\pm$  1.9-fold reduction) and oriens (1.5  $\pm$  0.8-fold reduction; Fig. 2h). In the oriens, walking significantly increased  $\theta$ -band power (6.7–8.3 Hz,  $146 \pm 24\%$  increase,  $P = 2 \times 10^{-5}$ , paired Student's  $t$ -test,  $n = 36$  cells) and decreased low-frequency power (2–6 Hz,  $37 \pm 5.4\%$  decrease,  $P = 4 \times 10^{-7}$ ), consistent with previously published local field potential recordings in freely walking animals<sup>19</sup>. In the PCL, walking did not significantly affect  $\theta$ -band power ( $23 \pm 18\%$  increase,  $P = 0.46$ , paired Student's  $t$ -test,  $n = 48$  cells) but significantly decreased low-frequency power ( $52 \pm 5.9\%$  decrease,  $P = 8 \times 10^{-7}$ ). Walking significantly decreased

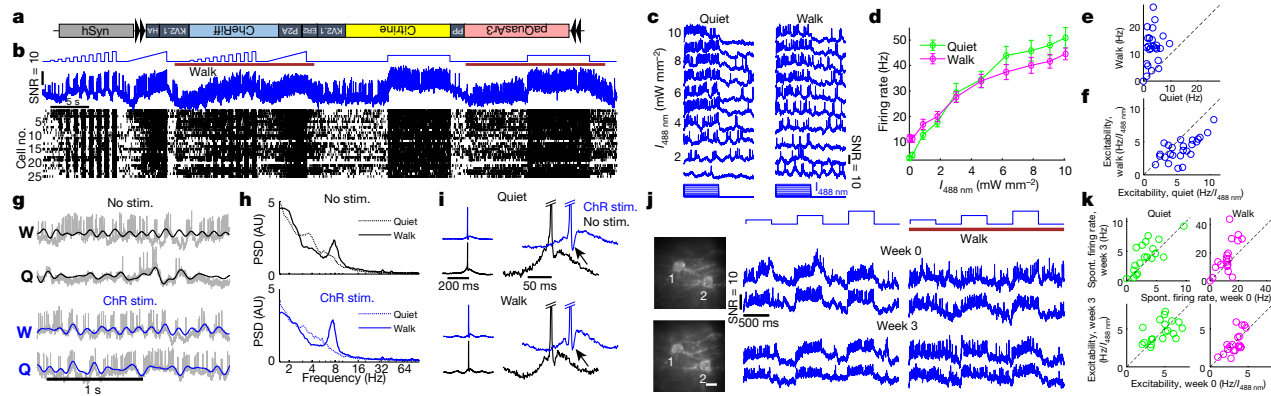


**Fig. 4 | Simultaneous optogenetic stimulation and voltage imaging in hippocampal SST cells in walking mice.** **a**, Schematic of the Optopatch construct for viral Cre-dependent co-expression of CheRiff-s and paQuasAr3-s. **b**, Top, protocol for optogenetic stimulation during quiet and walking. Middle, fluorescence of a single SST oriens cell showing optogenetically and behaviourally modulated firing. Bottom, spike raster from  $n = 25$  SST interneurons from 17 fields of views in  $n = 2$  mice. **c**, Optically recorded activity of a single oriens interneuron during 500-ms steps of optogenetic stimulation from 0 to  $10 \text{ mW mm}^{-2}$ . Left, quiet. Right, walking. **d**, Spike rate as a function of optogenetic stimulus strength ( $F-I$  curve) during quiet and walking (data are mean  $\pm$  s.e.m.,  $n = 25$  SST neurons in the oriens). **e**, Spontaneous spike rate (no optogenetic stimulation) during quiet and walking. **f**, Cell-by-cell excitability during quiet versus walking, measured as the slope of the  $F-I$  curve between 0 to  $8 \text{ mW mm}^{-2}$ . **g**, Subthreshold

dynamics during quiet and walking, with and without optogenetic stimulation (from the dataset shown in **b**). Grey, raw fluorescence. Blue and black, subthreshold dynamics (spikes digitally removed, bandpass-filtered 3–20 Hz). **h**, Effect of brain state and optogenetic stimulation on population-average power spectral density (PSD). **i**, Grand-average spike waveforms showing increased after-hyperpolarization during optogenetic stimulation (arrow). **j**, Two SST cells, recorded before and after a three-week interval. The full dataset is presented in Extended Data Fig. 10. **k**, Correlation of the firing rate and excitability ( $F-I$  slope) of  $n = 19$  SST cells recorded before and after a 3-week interval. Population-average firing rates slightly increased after 3 weeks (quiet,  $3.2 \pm 2.2$  to  $4.2 \pm 2.5$  Hz,  $P = 0.04$ ; walking,  $11.8 \pm 5.9$  to  $16.6 \pm 11.6$  Hz,  $P = 0.03$ ; paired Student's  $t$ -test; data are mean  $\pm$  s.d.). The  $F-I$  slope was stable between sessions (quiet,  $P = 0.82$ ; walking,  $P = 0.67$ ; paired Student's  $t$ -test).

the rate of complex spikes in the PCL ( $0.38 \pm 0.41$  Hz to  $0.09 \pm 0.25$  Hz, mean  $\pm$  s.d.,  $P = 4 \times 10^{-4}$ , paired Student's  $t$ -test).

Intercellular correlations in subthreshold voltage reflect shared synaptic inputs. In paired patch recordings in cortex in vivo, subthreshold oscillations have been decomposed into a shared correlated component and an uncorrelated residuum<sup>1,20–23</sup>. When more than two cells are measured simultaneously, it is possible to test for multiple subthreshold signals, shared among different subsets of cells<sup>24,25</sup>. We found that, in simultaneously recorded trios, the three pairwise cross-correlations can be distinctly different in shape and amplitude (Fig. 3a, e and Extended Data Fig. 9). In 10 fields of view in the PCL that contained more than 2 cells, the cell-to-cell cross-correlation functions were only correlated between different pairs by a mean of  $0.44 \pm 0.5$  during rest and  $0.32 \pm 0.48$  during walking (mean  $\pm$  s.d.,  $n = 54$  pairs of pairs), which establishes that multiple subthreshold signals exist in distinct sub-ensembles.

STAs of the fluorescence (Fig. 3c, g) reflect the relation between the subthreshold inputs and the spiking output. STA fluorescence of neighbouring cells (cross-STA)<sup>20,21</sup> were highly heterogeneous in both layers. Some pairs of cells showed nearly identical subthreshold components of self- and cross-STA, whereas others showed anti-correlated self- and cross-STA (Extended Data Fig. 9). The grand average cross-STA waveforms showed a strong  $\theta$ -rhythm component during walking, confirming that—on average— $\theta$ -rhythm inputs were strongly shared between cells (Fig. 3c, g). STA plots of the spike probability (Fig. 3d, h) revealed that in the PCL, when a cell spiked, its neighbours also had a slightly increased spike probability, which is probably a consequence of the shared subthreshold inputs. In the 150 ms around a spike, however, spiking cells had a period of suppressed spike probability, possibly owing to a cell-autonomous refractory period<sup>26</sup>. In the oriens, cells spiked at a relatively constant rate during the quiet period and at a rate modulated by the  $\theta$ -rhythm during walking.

Passive voltage imaging alone cannot distinguish the relative contributions of excitatory and inhibitory inputs to the membrane potential. Optogenetic depolarization of a cell can, in principle, resolve this ambiguity by amplifying the effect of inhibitory inputs and diminishing

the effect of excitatory inputs. We used a transgenic somatostatin-Cre (SST-Cre) mouse to target expression of paQuasAr3-s and soma-localized CheRiff, and imaged in the oriens<sup>27</sup> (Fig. 4a). Cells were stimulated with a variety of illumination intensities during rest and locomotion (Fig. 4b). Both red and blue illumination were patterned to illuminate only the cell bodies. For display purposes only, we subtracted the photoartefact of the blue light from the traces (Methods).

We collected a dataset of  $n = 25$  SST cells from  $n = 2$  mice. Single cells showed enhanced firing during walking (with no optogenetic stimulation) (Fig. 4b and Extended Data Fig. 10). We then measured the relation between the mean spike rate  $F$  and optogenetic stimulus strength,  $I$  ( $F-I$  curve) during quiet and walking (Fig. 4c, d). The slope of the  $F-I$  curve during walking was only  $75 \pm 32\%$  of the slope during quiet (mean  $\pm$  s.d.,  $n = 25$  cells,  $P = 3 \times 10^{-5}$ , paired Student's  $t$ -test; Fig. 4f), which reflects increased inhibition in the walking state.

To further analyse the change in excitatory to inhibitory balance during walking, we studied the influence of targeted optogenetic stimulation on the subthreshold dynamics. Similar to the broader oriens population (Fig. 2i), SST cells showed an increase in the  $\theta$ -band power (6.7–8.3 Hz) during walking ( $125 \pm 21\%$  increase (mean  $\pm$  s.d.),  $n = 25$  cells,  $P = 3 \times 10^{-5}$ , paired Student's  $t$ -test; Fig. 4h). Notably, in the presence of cell-targeted tonic optogenetic stimulation, these same cells showed a significantly larger increase in  $\theta$ -band power during walking ( $261 \pm 43\%$  increase,  $P = 4 \times 10^{-4}$ , paired Student's  $t$ -test;  $\theta$  power with or without ChR stimulation:  $P = 0.005$ , paired Student's  $t$ -test; Fig. 4h and Extended Data Fig. 10), which suggests that the  $\theta$ -rhythm in CA1 oriens interneuron is predominantly driven by oscillatory inhibition, possibly from the medial septum<sup>19,28</sup>.

Voltage-gated ion channels within each cell also contribute to both excitatory and inhibitory drives. We compared STA spike waveforms with and without optogenetic stimulation. In animals at rest, optogenetic depolarization markedly enhanced the spike after-hyperpolarization (Fig. 4i), revealing the role of voltage-gated  $K^+$  channels in governing the spike waveform.

To test the capability for chronic recordings, we imaged and then re-imaged SST cells at a three-week interval (Fig. 4j, k and Extended

Data Figs. 5, 10). Pair-wise comparisons of  $n = 19$  single cells at  $t = 0$  and  $t = 3$  weeks showed persistent correlations in firing rate during quiet ( $R = 0.74$ ,  $P = 3 \times 10^{-4}$ , Pearson's correlation), during walking ( $R = 0.67$ ,  $P = 2 \times 10^{-3}$ ) and in the effect of optogenetic stimulation on firing rate ( $F$ - $I$  slope) during quiet ( $R = 0.5$ ,  $P = 0.03$ ) and during walking ( $R = 0.67$ ,  $P = 0.001$ ).

GEVIs have the potential to be a powerful tool for studying neuronal dynamics in vivo in the context of behaviour, although they have currently been used mostly for technical demonstrations. To create a robust tool, improvements in the SNR in scattering brain tissue were required, which was established by improved membrane localization, photo-activation, soma-localized expression, soma-targeted illumination and algorithms for robust separation of in-focus signals from sources of crosstalk and background. A unique advantage of near-infrared GEVIs is their spectral compatibility with optogenetic actuators and green fluorescent protein (GFP)-based fluorescent reporters. The ability to investigate subthreshold dynamics and excitability over multiple days enables the study of changes in circuit dynamics associated with learning and memory.

### Online content

Any methods, additional references, Nature Research reporting summaries, source data, statements of data availability and associated accession codes are available at <https://doi.org/10.1038/s41586-019-1166-7>.

Received: 13 February 2018; Accepted: 13 February 2019;

Published online 1 May 2019.

- Petersen, C. C. H. Whole-cell recording of neuronal membrane potential during behavior. *Neuron* **95**, 1266–1281 (2017).
- Lee, A. K. & Brecht, M. Elucidating neuronal mechanisms using intracellular recordings during behavior. *Trends Neurosci.* **41**, 385–403 (2018).
- Lou, S. et al. Genetically targeted all-optical electrophysiology with a transgenic Cre-dependent Optopatch mouse. *J. Neurosci.* **36**, 11059–11073 (2016).
- Gong, Y. et al. High-speed recording of neural spikes in awake mice and flies with a fluorescent voltage sensor. *Science* **350**, 1361–1366 (2015).
- Yang, H. H. et al. Subcellular imaging of voltage and calcium signals reveals neural processing in vivo. *Cell* **166**, 245–257 (2016).
- Hochbaum, D. R. et al. All-optical electrophysiology in mammalian neurons using engineered microbial rhodopsins. *Nat. Methods* **11**, 825–833 (2014).
- Madisen, L. et al. Transgenic mice for intersectional targeting of neural sensors and effectors with high specificity and performance. *Neuron* **85**, 942–958 (2015).
- Miller, J. E. et al. Improved sensitivity in blue-membrane bacteriorhodopsin films. *Opt. Lett.* **24**, 1355–1357 (1999).
- Wagner, N. L., Greco, J. A., Ranaghan, M. J. & Birge, R. R. Directed evolution of bacteriorhodopsin for applications in bioelectronics. *J. R. Soc. Interface* **10**, 20130197 (2013).
- Häusser, M., Spruston, N. & Stuart, G. J. Diversity and dynamics of dendritic signaling. *Science* **290**, 739–744 (2000).
- Wu, C., Ivanova, E., Zhang, Y. & Pan, Z. H. rAAV-mediated subcellular targeting of optogenetic tools in retinal ganglion cells in vivo. *PLoS ONE* **8**, e66332 (2013).
- Baker, C. A., Elyada, Y. M., Parra, A. & Bolton, M. M. Cellular resolution circuit mapping with temporal-focused excitation of soma-targeted channelrhodopsin. *eLife* **5**, e14193 (2016).
- Buchanan, E. K. et al. Penalized matrix decomposition for denoising, compression, and improved demixing of functional imaging data. Preprint at <https://www.biorxiv.org/content/10.1101/334706v4> (2018).
- Klausberger, T. et al. Brain-state- and cell-type-specific firing of hippocampal interneurons in vivo. *Nature* **421**, 844–848 (2003).
- Harvey, C. D., Collman, F., Dombeck, D. A. & Tank, D. W. Intracellular dynamics of hippocampal place cells during virtual navigation. *Nature* **461**, 941–946 (2009).
- Bittner, K. C. et al. Conjunctive input processing drives feature selectivity in hippocampal CA1 neurons. *Nat. Neurosci.* **18**, 1133–1142 (2015).
- Epsztein, J., Brecht, M. & Lee, A. K. Intracellular determinants of hippocampal CA1 place and silent cell activity in a novel environment. *Neuron* **70**, 109–120 (2011).

- Varga, C., Golshani, P. & Soltesz, I. Frequency-invariant temporal ordering of interneuronal discharges during hippocampal oscillations in awake mice. *Proc. Natl Acad. Sci. USA* **109**, E2726–E2734 (2012).
- Buzsáki, G. Theta oscillations in the hippocampus. *Neuron* **33**, 325–340 (2002).
- Poulet, J. F. & Petersen, C. C. Internal brain state regulates membrane potential synchrony in barrel cortex of behaving mice. *Nature* **454**, 881–885 (2008).
- Gentet, L. J., Avermann, M., Matyas, F., Staiger, J. F. & Petersen, C. C. Membrane potential dynamics of GABAergic neurons in the barrel cortex of behaving mice. *Neuron* **65**, 422–435 (2010).
- Lampl, I., Reichova, I. & Ferster, D. Synchronous membrane potential fluctuations in neurons of the cat visual cortex. *Neuron* **22**, 361–374 (1999).
- Okun, M. & Lampl, I. Instantaneous correlation of excitation and inhibition during ongoing and sensory-evoked activities. *Nat. Neurosci.* **11**, 535–537 (2008).
- Briggman, K. L., Abarbanel, H. D. & Kristan, W. B. Jr. From crawling to cognition: analyzing the dynamical interactions among populations of neurons. *Curr. Opin. Neurobiol.* **16**, 135–144 (2006).
- Cunningham, J. P. & Yu, B. M. Dimensionality reduction for large-scale neural recordings. *Nat. Neurosci.* **17**, 1500–1509 (2014).
- Harris, K. D., Hirase, H., Leinekugel, X., Henze, D. A. & Buzsáki, G. Temporal interaction between single spikes and complex spike bursts in hippocampal pyramidal cells. *Neuron* **32**, 141–149 (2001).
- Bezaire, M. J. & Soltesz, I. Quantitative assessment of CA1 local circuits: knowledge base for interneuron–pyramidal cell connectivity. *Hippocampus* **23**, 751–785 (2013).
- Unal, G., Joshi, A., Viney, T. J., Kis, V. & Somogyi, P. Synaptic targets of medial septal projections in the hippocampus and extrahippocampal cortices of the mouse. *J. Neurosci.* **35**, 15812–15826 (2015).

**Acknowledgements** We thank M. S. Lee and V. Joshi for help with tissue culture, A. H. Gheorghie for help with spectroscopy experiments, N. Rollins and S. Brownsberger for technical help, L. Yapp for advice on hippocampal surgeries, A. Ruangkittisakul and K. Ballanyi for neuronal cultures, K. Podgorski for heating simulation code, G. Buzsáki and members of the Cohen laboratory for helpful discussions and D. Hochbaum, C. Straub, J. L. Saulnier, B. L. Sabatini, V. Kapoor and V. Murthy for help at early stages of the project. Y.A. was supported by fellowships from the Human Frontiers Science Program and the Edmund and Lili Safra Center for Brain Sciences. This work was supported by the Howard Hughes Medical Institute.

**Reviewer information** Nature thanks Kenneth Harris, Michael Hausser, Samuel Andrew Hires and the other anonymous reviewer(s) for their contribution to the peer review of this work.

**Author contributions** Y.A. performed the patch-clamp and imaging experiments in acute slices, cultured neurons and in vivo. J.J.K. performed patch-clamp measurements in HEK293T cells. Y.A. and Y.Z. performed protein engineering, with supervision by A.E.C. and R.E.C., respectively. Y.A. and D.B. performed spectroscopy experiments. Y.A. developed the imaging system with help from H.W., J.J.K., S.K. and V.P.S.L., L.M. and H.Z. developed and characterized the Ai155 Optopatch3 mice. M.A.M.-R. performed in utero electroporation, supervised by P.A. M.E.X. optimized and validated the penalized matrix decomposition–non-negative matrix factorization algorithm in collaboration with E.K.B., I.K., D.Z. and L.P.S.C. and C.D.H. shared unpublished reagents for soma targeting of opsins. K.J.W. helped with molecular biology. B.G. performed the heating simulation. S.L.F. designed the CheRiff–HA construct. Y.A. and A.E.C. designed the project, analysed data and wrote the manuscript. A.E.C. supervised all aspects of the project.

**Competing interests** A.E.C. is a founder of Q-State Biosciences. The other authors declare no competing interests.

### Additional information

**Extended data** is available for this paper at <https://doi.org/10.1038/s41586-019-1166-7>.

**Supplementary information** is available for this paper at <https://doi.org/10.1038/s41586-019-1166-7>.

**Reprints and permissions information** is available at <http://www.nature.com/reprints>.

**Correspondence and requests for materials** should be addressed to A.E.C.

**Publisher's note**: Springer Nature remains neutral with regard to jurisdictional claims in published maps and institutional affiliations.

© The Author(s), under exclusive licence to Springer Nature Limited 2019

## METHODS

**Protein engineering. Screening pipeline.** Performance of a GEVI depends on several independent parameters: brightness, sensitivity, speed of response, expression level and membrane trafficking. QuasAr2 showed excellent sensitivity and speed<sup>6</sup>, but dim fluorescence and poor membrane trafficking in vivo, limiting application of this sensor in vivo (Extended Data Fig. 1). Trafficking efficiency and expression levels can differ markedly between cell types and growth conditions, so it is important to test candidate GEVIs in neurons and ultimately in vivo.

We used the SNR for single spikes in cultured neurons as the screening parameter. The SNR integrates all relevant molecular features and is the parameter that is most relevant to applications in vivo. To facilitate rapid evaluation of constructs we used the Optopatch configuration for simultaneous optical stimulation and optical measurement of action potentials, comprising bicistronic expression of the candidate GEVI with the blue-shifted channelrhodopsin, CheRiff, using a P2A peptide<sup>6</sup>.

The starting material comprised QuasAr2 fused to dark mOrange2 (QuasAr2-dmOrange2-TS-ER2) driven by the CamKII promoter. It has previously been found that the presence of an appended fluorescent fusion is beneficial for trafficking<sup>6</sup>, but we wished to reserve the spectrum for other uses, so we introduced the mutation Y71A into the mOrange2 backbone to destroy the chromophore<sup>3,29</sup>. TS represents the trafficking sequence from *K<sub>v</sub>2.1*<sup>30</sup> and ER2 represents the endoplasmic reticulum export signal FCYENEV<sup>30</sup>.

QuasAr variants were then transfected into primary neurons using the calcium phosphate transfection method and tested for spike SNR using blue-light stimulation. Membrane trafficking in vivo was often worse than in vitro, thus constructs that showed SNR improvements in cultured primary neurons were then expressed in vivo using in utero electroporation and tested for spike SNR in acute brain slices (Extended Data Fig. 1).

**QuasAr3.** The primary goal in developing QuasAr3 was to solve the membrane trafficking problem. We tested multiple modifications. Some other microbial rhodopsins (for example, CheRiff, ChR86 and ChR1<sup>31</sup>) showed good membrane trafficking in the rodent brain in vivo, so we explored chimaeras comprising N-terminal fusions derived from these microbial rhodopsins. The N terminus was added either appended to the QuasAr N terminus or added after truncation of the first 16 residues from the QuasAr N terminus. We also tried the N-terminal LUCY and LUCY-Rho tags, which were shown to improve the surface expression of olfactory receptor<sup>32</sup> and multiple repeats of the TS sequence<sup>30</sup>. Most modifications had neutral or negative effects on the SNR. Adding a second TS sequence in the linker between QuasAr2 and mOrange improved the spike SNR in vitro by 28%. Concatenating three TS sites instead of one at the C terminus further improved SNR in vitro by 17% (Extended Data Fig. 1d–f). Mutating a putative ubiquitination site in an intracellular loop (K171R) resulted in higher expression levels, quantified by dividing the QuasAr fluorescence with the fluorescence of the GFP fused to the co-expressed CheRiff (Extended Data Fig. 1g).

In parallel to rational designs, we used a hierarchical screening approach for rapid evaluation of membrane trafficking and brightness of QuasAr point-mutant and linker libraries (Extended Data Fig. 1c). We found that lentiviral gene delivery was superior to conventional lipid-based transfection in primary cultured neurons as measured by homogeneity of expression, neuronal morphology and homogeneity of membrane trafficking. Therefore, we developed a screening strategy in which constructs that showed good brightness in *Escherichia coli* could immediately be packaged in lentiviral vectors and tested in neurons, without laborious recloning. We inserted a putative prokaryotic promoter sequence BBAJ23101 (TTTACAGCTAGCTCAGTCCTAGGTATATGC) and an *E. coli* ribosome-binding site (AAAGAAGAGAAA) between the CAMKII promoter and the Kozak sequence of plasmid FCK-Arch-GFP (Addgene 22217)<sup>33</sup>. The resulting vector is termed FCK\_DuEx1.0 for gene expression in both prokaryotic and eukaryotic cells as well as lentivirus production.

We created libraries of QuasAr2 fused to eGFP, citrine, mKate or mRuby with a linker containing two randomized amino acids between QuasAr2 and the fluorescent protein fusion. For library screening, *E. coli* colonies were transformed with linker libraries in FCK\_DuEx1.0. The colonies with the brightest fluorescence were picked for lentivirus production in HEK293T cells and secondary screening in primary neuronal cultures. For lentivirus production, HEK293T cells were co-transfected with the QuasAr variants in FCK\_DuEx1.0, along with packaging plasmids pCMV-dR8.2 dvpr (Addgene 8455) and pCMV-VSV-G (Addgene 8454). The medium from the HEK293T cell culture was collected 48 h after transfection and 10% of the lentivirus-containing medium was added into the primary hippocampal neuronal cultures for transduction. After 2–5 days, the membrane trafficking of QuasAr mutants was evaluated using fluorescence microscopy. The best constructs in this screen included citrine as the fluorescent protein fusion with four different two amino acids linkers—GE, GP, PP or PT. These constructs were then cloned in the Optopatch configuration and tested for spike SNR as described above. Two of these linkers, PP and PT, showed better SNR compared with QuasAr2–mOrange (Extended Data Fig. 1e).

We next combined the best modifications into a new construct: QuasAr2(K171R)-TS-citrine-TS-TS-TS-ER2, which we call QuasAr3. We packaged QuasAr3 into an adeno-associated virus (AAV) and validated its performance in acute slices (Extended Data Fig. 1h–j).

**paQuasAr3.** We explored the effects of previously described Arch point mutations T27A, V59A, T99C, P196S, I129V, I129T and A225M<sup>34</sup> on membrane trafficking, brightness and sensitivity of QuasAr1 and QuasAr2 using the hierarchical screening pipeline described above. We introduced these mutations separately into QuasAr2–citrine, and estimated brightness by expressing these constructs in primary neurons and dividing the QuasAr fluorescence by the citrine fluorescence. Initially it seemed that none of the mutations improved the QuasAr brightness. However, when we tested mutation V59A for spike SNR using blue-light optogenetic stimulation, we found that fluorescence of the V59A mutant was potentiated by blue light. The photoactivation property of the V59A mutant may be related to the photoswitching property observed in the homologous bacteriorhodopsin mutant (V49A)<sup>9</sup>.

To our surprise, we found that the V59A mutation led to near-perfect membrane trafficking. This improved trafficking may be related to the enhanced thermal stability observed in the homologous bacteriorhodopsin mutant<sup>9</sup>. The photoactivation property, combined with the excellent trafficking, motivated us to further characterize QuasAr3(V59A) (Fig. 1 and Extended Data Fig. 3).

**paQuasAr3-s and CheRiff-s.** The trafficking sequence of the *K<sub>v</sub>2.1* channel was previously shown to restrict the expression channelrhodopsin 2 to the soma and proximal dendrites<sup>11,12</sup>. To produce soma-localized paQuasAr3 and CheRiff, we removed all of the *K<sub>v</sub>2.1* TS and introduced the *K<sub>v</sub>2.1* sequence: QSQPILNTKEMAPQSKPPEELEMSSMPSPVAPLPAETEGVIDMRMSSIDSFI SCATDFPEATRF in the linker, at the C terminus or in both positions. In the QuasAr construct with a single *K<sub>v</sub>2.1* sequence in the C terminus, we used PP for the linker (see above). CheRiff was directly fused with GFP. These six constructs were then expressed in primary hippocampal neurons and visually inspected for localization. For both CheRiff and paQuasAr3, expression was most somatrestricted when the *K<sub>v</sub>2.1* motif was at the C terminus. These constructs were further characterized both in slices and in vivo (Fig. 2–4 and Extended Data Fig. 3). **Spectroscopic studies.** To investigate the spectroscopic properties of the QuasAr3 and paQuasAr3 proteins, we expressed them in *E. coli* as previously described<sup>6</sup>. In brief, *E. coli* cultures were grown overnight in liquid LB medium with 200  $\mu\text{g ml}^{-1}$  ampicillin. The next day, the cultures were supplemented with 50  $\mu\text{M}$  all-*trans*-retinal and 0.1% arabinose and incubated for 4 h at 37 °C. Cell pellets were collected by centrifugation and kept at –80 °C until use. We measured the excitation and photoactivation spectra using a previously described microscope equipped with a wavelength-tunable supercontinuum light source and an EMCCD detector<sup>35</sup>.

**Optical systems. Imaging HEK293T cells and primary neurons.** Experiments were conducted on a custom-built inverted fluorescence microscope equipped with 405-nm, 488-nm, 532-nm and 640-nm laser lines and a scientific CMOS camera (Hamamatsu, ORCA-Flash 4.0). Laser beams were combined using dichroic mirrors and sent through an acousto-optic tunable filter (Gooch and Housego, TF525-250-6-3-GH18A) for temporal modulation of the intensity of each wavelength. The beams were then expanded and focused onto the back-focal plane of a 60 $\times$  water immersion objective, 1.2 numerical aperture (NA) (Olympus UIS2 UPlanSApo 60 $\times$ /1.20 W). Imaging of fluorescent proteins was performed at illumination intensities of 20–40  $\text{mW mm}^{-2}$ . Imaging of QuasAr fluorescence was performed at an illumination intensity of 4  $\text{W mm}^{-2}$ . Stimulation of CheRiff was performed at an illumination intensity of 0.4–1.2  $\text{mW mm}^{-2}$ . For fast data acquisition, a small field of view around the cell of interest was chosen at the centre of the camera to achieve a frame rate of 1 kHz.

**Imaging acute slices and live mice.** Experiments were conducted on a custom-built upright fluorescence microscope equipped with 488-nm and 640-nm laser lines and a scientific CMOS camera (Hamamatsu, ORCA-Flash 4.0). The 488-nm line was sent through an acousto-optic tunable filter (Gooch and Housego, 48058-2.5-55) for intensity modulation, and then expanded and focused onto the back-focal plane of the objective.

In the first generation of the microscope, we used a 140-mW, 640-nm laser expanded to a single  $\sim 50\text{-}\mu\text{m}$  circular spot, and a 20 $\times$  1.0 NA objective (Olympus XLUMPLFLN 20 $\times$ /1.0 W). This configuration was used for the olfactory bulb in vivo experiments (Fig. 1h). Data were acquired on a small field of view around the cell of interest at a frame rate of 1 kHz.

In the second generation of the microscope, we used an 8-W, 640-nm diode bar laser (DILAS, MB-638.3-8C-T25-SS4.3) and patterned the illumination using a DMD (Vialux, V-7000 UV, 9515) to illuminate specific sub-cellular structures and to avoid illuminating interstitial regions of the brain slice. We used a 16 $\times$  0.8 NA objective with 3-mm working distance (Nikon, CFI75 LWD 16 $\times$ /0.8 W). Sampling rate was 1 kHz. This configuration was used for the single-cell in vivo measurements in the hippocampus (Fig. 1i–k).

In the third generation of the microscope, we patterned both the 488-nm and 640-nm lasers to achieve overlapping red and blue spots in the sample. The beams were then combined on a dichroic beam splitter and aligned to be side-by-side and propagating parallel. The combined beam was then sent to a DMD, so half of the DMD patterned one wavelength and half of the DMD patterned the other wavelength. The two wavelengths were then split and recombined with a pair of dichroic mirrors to form a single beam with independently patterned blue- and red-light excitation (Fig. 2c). Cylindrical lenses were used to correct for aberrations introduced by slight warping of some dichroic mirrors.

The patterned epi-illumination was combined with a custom-built scanning two-photon system. The visible and near-infrared beams were combined using an 875-nm long-pass dichroic mirror (Semrock). A 532-nm notch dichroic mirror (Semrock) directed green emission (from citrine or GFP) to a photomultiplier, while near-infrared fluorescence (from QuasAr) was sent to a Hamamatsu sCMOS camera. This configuration was used for all multicellular recordings in the hippocampus *in vivo* (Figs. 2–4) using a  $25\times 1.0$  NA objective with 4-mm working distance (Olympus, XLPLN25XSVM2). Red laser intensity was  $12\text{ W mm}^{-2}$  and the sampling rate was 1 kHz.

This configuration was also used for the patch-clamp experiments in slices (Fig. 1e–j and Extended Data Figs. 1j, 3i–k) with a  $20\times$  objective (Olympus XLUMPLFN,  $20\times/1.0$  W), red laser intensity was  $12\text{ W mm}^{-2}$  and the sampling rate was 1 kHz, and for measurements from brain slices of transgenic mice (Extended Data Fig. 2) at a 500-Hz sampling rate.

**Primary neuronal culture and gene delivery.** All procedures involving animals were in accordance with the National Institutes of Health Guide for the care and use of laboratory animals and were approved by the Harvard University Institutional Animal Care and Use Committee.

Hippocampal neurons from postnatal day 0 (P0) rat pups were dissected and cultured on rat glial monolayers as previously described<sup>6</sup>. In brief, P0 neurons were plated in neurobasal-based medium (NBAciv4, BrainBits) at a density of 30,000–40,000 cells per  $\text{cm}^2$  on the pre-established glial monolayers. At one day *in vitro* (DIV), cytarabine was added to the neuronal culture medium at a final concentration of  $2\ \mu\text{M}$  to inhibit further glial growth.

Neurons were transfected between DIV 7 and DIV 10 using the calcium phosphate transfection method. Measurements on neurons were taken between DIV 14 and DIV 18.

**Imaging and electrophysiology in HEK293T cells and primary neurons.** HEK293T cells (ATCC; CRL-11268) were cultured and transfected as previously described<sup>6</sup>. In brief, HEK293T cells were grown at  $37^\circ\text{C}$ , 5%  $\text{CO}_2$ , in DMEM supplemented with 10% FBS and penicillin–streptomycin. Cells tested negative for mycoplasma. Cells were transfected with GEVI constructs under the upstream CMV promoter of the FCK plasmid. Subsequently, 200–400 ng of plasmid DNA was transfected using Transit 293T (Mirus) following the manufacturer's instructions and assayed 48 h later. The day before recording, cells were replated onto Matrigel-coated glass-bottom dishes (In Vitro Scientific) at a density of around 10,000 cells per  $\text{cm}^2$ .

All imaging and electrophysiology experiments were performed in extracellular buffer containing (in mM): 125 NaCl, 2.5 KCl, 3 CaCl<sub>2</sub>, 1 MgCl<sub>2</sub>, 15 HEPES, 30 glucose (pH 7.3) and adjusted to 305–310 mOsm with sucrose. A gap junction blocker, 2-aminoethoxydiphenyl borate ( $50\ \mu\text{M}$ , Sigma-Aldrich), was added to HEK293T cells to eliminate electrical coupling between cells. Primary neurons were supplemented with excitatory synaptic blockers (either  $20\ \mu\text{M}$  NBQX or  $20\ \mu\text{M}$  CNQX; both from Tocris).

Optopatch measurements and the simultaneous whole-cell patch-clamp and fluorescence recordings were acquired on the custom-built, inverted epifluorescence microscope described above. For simultaneous electrophysiology and imaging, filamented glass micropipettes (WPI) were pulled to a tip resistance of 5–10 M $\Omega$ , and filled with internal solution containing (in mM): 125 potassium gluconate, 8 NaCl, 0.6 MgCl<sub>2</sub>, 0.1 CaCl<sub>2</sub>, 1 EGTA, 10 HEPES, 4 Mg-ATP and 0.4 Na-GTP (pH 7.3); adjusted to 295 mOsm with sucrose. Pipettes were positioned with a Sutter MP285 manipulator. Whole-cell, voltage- and current-clamp recordings were acquired using a Multiclamp 700B amplifier (Molecular Devices), filtered at 2 kHz with the internal Bessel filter and digitized with a National Instruments PCIE-6323 acquisition board at 10 kHz.

**Gene targeting in embryonic stem (ES) cells and generation of knock-in Cre-dependent reporter mice.** To generate the Ai155 targeting vector, Optopatch3 comprising QuasAr2(K171R)-TS-citrine-TSX3-ER2-P2A-CheRiff-TS-HA was inserted into the Cre-dependent TIGRE 2.0 construct<sup>36</sup>. Gene targeting was performed at the Allen Institute for Brain Science. Targeting of the transgene cassettes into the TIGRE locus was accomplished by Flp-recombinase mediated cassette exchange using circularized targeting vector, a CAG-FlpE vector (Open Biosystems) and a Flp recombinase landing pad ES cell line derived from G4 cells<sup>7</sup>. Correctly targeted ES cells were identified by PCR, qPCR and Southern blots. ES clones were karyotyped and verified to be chromosomally normal.

ES clone injection was performed at the Harvard University Genetic Modification Facility. Optopatch-positive ES clones were injected into C57BL/6J blastocysts to obtain chimeric mice. Chimeric mice were bred with C57BL/6J mice to obtain *F<sub>1</sub>* *Floxedoptch<sup>+/−</sup>* mice. The Ai155 mouse line is on a mixed C57BL/6J;C57BL/6N genetic background. The Ai155 mouse line has been deposited in Jackson laboratory with stock no. 029679.

Ai155 mice were crossed with the following Cre driver lines: CKII-Cre (gift from V. Murthy), SST-IRES-Cre (JAX 013044) and Rbp4-Cre (MMRRC-031125-UCD, gift from B. L. Sabatini).

**Genotyping.** The presence of QuasAr3 was determined with the primer pair: 5'-GCTGGTCTCCAACCTCCTAATC-3' and 5'-CTGTATCTGGCTATGGC CG-3'. A 1.07-kb amplicon indicated the presence of the gene. Homozygous mutant insertion was determined with the primer triplets: 5'-GTGTAGCCCTG GCTTTTCTG-3', 5'-GAACTCACAGTGGCCAGTCA-3' and 5'-TCCCTGGCA CAACGTAAG-3'. These yielded a 295-bp amplicon for the mutant band and a 468-bp amplicon for the wild-type band.

**Imaging and electrophysiology in acute slices. *In utero* electroporation.** *In utero* electroporation was performed in timed pregnant CD-1 mice as previously described<sup>37</sup>. The day of vaginal plug was designated as embryonic day 0.5 (E0.5), while the day of birth was designated as P0. In brief, 1  $\mu\text{l}$  of endonuclease-free purified DNA ( $3.75\ \mu\text{g}\ \mu\text{l}^{-1}$  comprising  $2.75\ \mu\text{g}\ \mu\text{l}^{-1}$  of the candidate GEVI construct and  $1\ \mu\text{g}\ \mu\text{l}^{-1}$  of tdTomato control) in sterile PBS mixed with 0.005% Fast Green was injected into the lateral ventricle of E14.5 mice under ultrasound guidance (Vevo 770, VisualSonics). Five 35-V pulses of 50-ms duration at 1-s intervals were delivered outside the uterus in appropriate orientation using 1-cm diameter platinum electrodes and a CUY21EDIT square-wave electroporator (Nepa Gene). Tested constructs were co-electroporated with either CBIG-tdTomato plasmid (gift from J. Macklis) or pCAG-GFP (gift from C. Cepko, also available as Addgene 11150) for visual identification of electroporated embryos using a fluorescence stereoscope.

**AAV virus preparation.** Constructs were cloned into an AAV transfer plasmid either with hSyn promoter (Addgene 51697) or for Cre-dependent expression with the CAG promoter (Addgene 22222)<sup>33</sup>. To pack the Cre-dependent Optopatch constructs into the 4.5-kb size limitation of AAVs, we had to modify both the construct and the transfer plasmid. First, we replaced the GFP fusion of CheRiff with a short HA tag. Second, we used a Cre-dependent transfer plasmid with an hSyn promoter instead of CAG (Addgene 44362)<sup>38</sup>. Third, we swapped the 480-bp bGH poly(A) sequence with 120-bp SV-40 poly(A). Viruses were produced by the Gene Transfer Vector Core at Massachusetts Eye and Ear Infirmary & Schepens Eye Research Institute (MEEI). All experiments used AAV serotype 2/9. All AAV plasmids were deposited with Addgene as follows: hSyn-QuasAr3-mOrange (Extended Data Fig. 1h, Addgene 107705), hSyn-QuasAr3-citrine-P2A-CheRiff (Extended Data Fig. 1h, Addgene 107700), CAG-FLEX-QuasAr3-citrine (Extended Data Figs. 1i–j, 3i, Addgene 107701), CAG-FLEX-paQuasAr3-citrine (Fig. 1d–k and Extended Data Fig. 3i, Addgene 107702), CAG-FLEX-paQuasAr3-s-citrine (Figs. 2, 3 and Extended Data Figs. 3k, 4, 6–9, Addgene 107703), hSyn-Dio-paQuasAr3-s-citrine-P2A-CheRiff-s (Fig. 4, Extended Data Figs. 5, 10, Addgene 107704).

**Virus injection for acute slice measurements.** For acute brain slice experiments, we injected AAV virus in C57BL/6 P0–P1 mice of either sex. Virus was diluted and injected at final titres of  $1\times 10^{13}$  genome copies (GC)  $\text{ml}^{-1}$ . To achieve sparse expression, Cre-dependent constructs were mixed with hSyn-Cre virus at final titres of  $1$  to  $5\times 10^{10}$  GC  $\text{ml}^{-1}$ .

P0–P1 pups were cryo-anaesthetized and immobilized dorsal side up under a stereotaxic setup. Injections were made using home-pulled micropipettes (Sutter P1000 pipette puller), mounted in a microinjection pump (World Precision Instruments, Nanolitre 2010) controlled by a microsyringe pump controller (World Precision Instruments, Micro4). The micropipette was positioned using a stereotaxic instrument (Stoelting). Pups were injected in the left hemisphere, 0.9 mm lateral and 0.9 mm anterior to lambda. Starting at a depth of 1.0 mm beneath the surface of the skull, virus injections ( $40\ \text{nl}$ ,  $5\ \text{nl s}^{-1}$ ) were performed at 0.1 mm increments as the pipette was withdrawn. Pups were placed back in their home cage once they were awake.

**Acute slice preparation.** Acute brain slices were prepared from P14–P28 mice as previously described<sup>3</sup>. In brief, mice were anaesthetized with isoflurane and then subjected to intracardiac perfusion with ice-cold slicing solution containing (in mM): 110 choline chloride, 2.5 KCl, 1.25 NaH<sub>2</sub>PO<sub>4</sub>, 25 NaHCO<sub>3</sub>, 25 glucose, 0.5 CaCl<sub>2</sub>, 7 MgCl<sub>2</sub>, 11.6 Na-ascorbate and 3.1 Na-pyruvate and saturated with carbogen (95% O<sub>2</sub>, 5% CO<sub>2</sub>). Mice were then decapitated and the brains were rapidly dissected and sliced into 300- $\mu\text{m}$  coronal sections using a vibratome (Leica VT 1200S). Mice younger than P21 were directly decapitated without intracardiac perfusion. Slices were incubated for 45 min at  $34^\circ\text{C}$  in a carbogenated artificial cerebrospinal fluid (ACSF) containing (in mM): 127 NaCl, 2.5 KCl, 1.25 NaH<sub>2</sub>PO<sub>4</sub>, 25 NaHCO<sub>3</sub>, 25 glucose, 2 CaCl<sub>2</sub> and 1 MgCl<sub>2</sub>. The osmolarity of all solutions was adjusted to 300–310 mOsm and the pH was maintained at 7.3 under constant bubbling with carbogen.

**Imaging and electrophysiology in acute slices.** Acute slices of either the visual cortex or CA1 were imaged on a custom-built upright microscope as described above. Measurements were conducted in carbogen-saturated ACSF at room temperature in slices from transgenic mice or at around 31 °C for all patch-clamp experiments. ACSF was perfused at a rate of 2 ml min<sup>-1</sup>. For simultaneous imaging and whole-cell patch-clamp measurements, filamented glass micropipettes (WPI) were pulled to a tip resistance of 4–6 MΩ, and filled with internal solution containing (in mM): 125 potassium gluconate, 8 NaCl, 0.6 MgCl<sub>2</sub>, 0.1 CaCl<sub>2</sub>, 1 EGTA, 10 HEPES, 4 Mg-ATP and 0.4 Na-GTP (pH 7.3); adjusted to 295 mOsm with sucrose. Pipettes were positioned with a Sutter MP285 manipulator. Whole-cell current-clamp recordings were acquired using a MultiClamp 700B amplifier (Molecular Devices), filtered at 2 kHz with the internal Bessel filter and digitized with a National Instruments PCIE-6323 acquisition board at 10 kHz. Action potentials were evoked by 10-s ramps of current injection from 0 to 200 pA. To evoke subthreshold post-synaptic potentials, we positioned a concentric bipolar electrode (FHC) in cortical layer 5–6 and delivered trains of stimuli (10 × 100 μs at 2 Hz). Stimulus strength was ramped during the trains and was adjusted to evoke subthreshold post-synaptic potentials.

**Confocal imaging.** Acute slices were fixed in 4% paraformaldehyde and confocal fluorescence imaging was performed on an Olympus FV1000 confocal microscope at the Harvard Center for Brain Sciences microscopy facility.

**Cranial windows, virus injections, training and in vivo imaging.** *Virus injection and cranial window surgery.* In brief, 10–18-week-old C57BL/6 or heterozygous SST-Cre mice (male and female) were deeply anaesthetized with 2% isoflurane and maintained with around 1% isoflurane throughout the surgery. The skull was exposed and thoroughly dried and a 3-mm round craniotomy was opened using a biopsy punch (Milten). For imaging of the olfactory bulb, the craniotomy covered both olfactory bulbs as previously described<sup>39</sup>. For CA1 imaging, the craniotomy centre was 1.8 mm lateral, 2.0 mm caudal of bregma. Virus was then injected in 1–3 locations in the centre of the craniotomy.

For single-cell measurements with paQuasAr3 (Fig. 1), sparse expression was achieved by mixing CAG-FLEX-paQuasAr3 AAV virus (final titre  $2 \times 10^{13}$  GC ml<sup>-1</sup>) with hSyn-Cre virus (final titre  $2 \times 10^{10}$  to  $1 \times 10^{11}$  GC ml<sup>-1</sup>). For dense expression of paQuasAr3-s, we used low titre CAG-FLEX-paQuasAr3 virus (final titre  $6 \times 10^{11}$  GC ml<sup>-1</sup>) or hSyn-DiO-paQuasAr3-s-P2A-CheRiff-s (final titre  $1.6 \times 10^{12}$  GC ml<sup>-1</sup>), mixed with higher titre CKII(0.4)-Cre virus (UPenn vector core, final titre  $7 \times 10^{11}$  GC ml<sup>-1</sup>). Injections were made using home-pulled micropipettes (Sutter P1000 pipette puller), mounted in a micro-injection pump (World Precision Instruments, Nanolitre 2010) controlled by a microsyringe pump controller (World Precision Instruments, Micro4). The micropipette was positioned using a stereotaxic instrument (Stoelting Digital Mouse Stereotaxic Instrument). For CA1 expression, injections were made –1.5 mm to –1 mm from dura, at 0.1-mm increments (40 nl per depth, 5 nl s<sup>-1</sup>). For olfactory bulb expression, injections were made from –0.4 to 0 mm from dura at 0.1-mm increments (40 nl per depth, 5 nl s<sup>-1</sup>). Brain surface was kept moist with saline throughout the injection.

In the olfactory bulb, a 3-mm round no. 1 cover glass (Harvard Apparatus) was then placed on the surface of the olfactory bulb, and sealed with cyanoacrylate and dental cement (C&B Metabond). A titanium bar was glued behind the window, the skin was sutured and the animal was allowed to recover.

The procedure for imaging in CA1 followed a previously described protocol<sup>40</sup>. In brief, a cannula was prepared before the surgery and comprised a 1.5-mm segment of a 3-mm outer diameter thin-walled stainless steel tube (MicroGroup). A 3-mm diameter no. 1 round cover glass (Harvard Apparatus) was cemented to one end of the tube using UV-curable adhesive (Norland Products) and cured for at least 5 min on a standard laboratory UV table. Following hippocampal virus injection, we removed the dura, and then slowly aspirated the cortex while continuously irrigating with saline until bleeding stopped. After exposure of the external capsule, a small region of the capsule in the centre was gently removed, exposing the CA1 surface. To reduce brain motion during locomotion, in some of the animals a small amount of Kwiksil (WPI) was applied to the surface of the brain. The cannula was then inserted and cemented to the skull with dental cement (C&B Metabond). After the cannula cured, a titanium head plate (as previously described<sup>41</sup>) was glued around the cannula and any exposed skull was covered with dental cement. Animals were returned to their home cage for recovery and treated for 3 days with carprofen (5 mg kg<sup>-1</sup>) and buprenorphine (0.1 mg kg<sup>-1</sup>) twice a day. To avoid damage to the implant, mice were housed in separate cages.

**Imaging anaesthetized animals.** Imaging typically started 3 weeks after surgery. Mice were lightly anaesthetized (0.7–1% isoflurane) and head-fixed under the upright microscope (see above) using the titanium head plate. Eyes were kept moist using ophthalmic eye ointment. Body temperature was continuously monitored and maintained at 37 °C using a heating pad (WPI). A typical imaging session lasted 1–2 h, after which the animals quickly recovered and were returned to their home cage.

**Motorized treadmill.** A custom-built treadmill was composed of two 3D printed plastic wheels (5-cm wide, 10-cm in diameter). We used a 5-cm wide, 180-cm long velvet belt (McMaster Carr 88015K1). Treadmill speed was regulated using a computer-controlled small electric motor (Pololu 3042). Linear speed was 5 to 10 cm s<sup>-1</sup>.

**Imaging awake, walking animals.** Head-fixed animals were imaged while walking on a custom-built motorized treadmill. Before imaging sessions started, mice were habituated to head restraint and walking by training them at least three times, every 24 h, for 15–30 min. During each training session mice were first habituated to head restraint until completely relaxed, and then started walking on the treadmill. Each walking period lasted 1 min followed by at least 2 min of rest. Walking speed was 5 to 10 cm s<sup>-1</sup>. To adjust mice to imaging conditions, at least one training session took place under the microscope with the objective on top of the cranial window. Awake animals were imaged three weeks to three months after virus injection without any detectable effects on cell health. More than 95% of SST cells could be reidentified and rerecorded after a 3-weeks interval ( $n = 2$  mice).

For experimental runs, we first used a protocol of 10-s rest following by three 15-s periods of increased speed (5, 7.5 and 10 cm s<sup>-1</sup>) followed by additional 10-s rest (65 s in total, Extended Data Fig. 8). We observed that the difference in firing patterns was more starkly different between rest and walking than between different walking speeds, so we switched to a protocol of 15-s rest followed by 15-s walking at 10 cm s<sup>-1</sup> repeated twice (60 s in total). In each field of view (FOV), we repeated the protocol two to five times. Imaging session lasted up to 1 h and then animals were returned to their home cages.

For combined voltage imaging and optogenetic stimulation (Fig. 4 and Extended Data Fig. 10), we performed a 75-s protocol, composed of 500-ms steps of blue light at successively greater intensities (nominally 0.2–10 mW mm<sup>-2</sup>, not accounting for light scatter), 5-s ramps of blue light (0–10 mW mm<sup>-2</sup>) and 8-s periods of constant illumination (5 mW mm<sup>-2</sup>), repeated during quiet and walking epochs.

**Data analysis. Statistics.** Statistical tests were performed using standard MATLAB functions (MathWorks). For two-sample comparisons of a single variable, a two-sided Student's *t*-test (paired or unpaired) was used unless otherwise noted. The experiments were not randomized, and the investigators were not blinded to the experimental condition. Sample size was based on reports in related literature and was not predetermined by calculation.

**Extracting fluorescence from single-cell videos.** First, an estimate of the photobleaching baseline was constructed from the mean intensity of the whole FOV by applying a sliding minimum filter, followed by a sliding mean filter. Each frame of the video was then divided by this baseline. Fluorescence values were extracted from corrected videos in one of two ways. When single cells were well isolated from other fluorescent sources, we used the maximum likelihood pixel weighting algorithm that has previously been described<sup>42</sup>. In brief, the fluorescence at each pixel was correlated with the whole-field average fluorescence. Pixels that showed stronger correlation to the mean were preferentially weighted. This algorithm automatically found the pixels that contained the most information and de-emphasized background pixels. Alternatively, we used a user-defined region of interest and calculated fluorescence from the unweighted mean of pixel values within this region. For calculations of  $\Delta F/F$ , background fluorescence from a cell-free region was subtracted from the baseline fluorescence of the cell.

**Sub-frame interpolation of action potential timing (SNAPT).** Dendritic propagation spike width and delay were calculated using the SNAPT algorithm as previously described<sup>6</sup>. In brief, spikes were identified from the whole-cell fluorescence trace. Spike timing was used to construct a STA video. The mean spike waveform was then used as a template and fit to the spike waveform at each pixel, using as fitting parameters: vertical offset, amplitude, time shift and width (uniform dilation in time). The time-shift and width parameters are displayed in Fig. 1k.

**Extracting fluorescence and subcellular voltages.** Inference of subthreshold voltages required explicit steps to account for possible contamination from motion artefacts, possible crosstalk between nearby cells of which the true subthreshold fluctuations were correlated and possible crosstalk from out-of-focus background created by one or more cells.

**Extracting fluorescence from sparse multicellular videos in behaving animals (oriens data).** Videos were first corrected for motion using the NoRMCorre algorithm<sup>43</sup>. Videos were then corrected for photobleaching by dividing the video by an exponential fit of the mean fluorescence. Activity-based image segmentation was performed on the spiking component of the signal. To remove subthreshold signals for segmentation purposes, videos were high-pass-filtered in time with a 50-Hz high-pass filter. Videos were then segmented semi-automatically using principal component analysis followed by time-domain independent component analysis (PCA/ICA)<sup>44</sup>. ICA produces an arbitrary number of candidate cells. We set the maximum number of sources to 15 and then further eliminated traces that did not correspond to cells by manually inspecting the traces and corresponding spatial maps. In some cases, we divided the video into sub-videos based on patterns of illumination from the DMD masks (Fig. 2d), and performed the PCA/ICA

analysis separately in each sub-video. The spatial masks from PCA/ICA were then applied to the videos without high-pass-filtering to extract fluorescence traces that included subthreshold dynamics.

*Extracting fluorescence from dense multicellular videos in behaving animals (PCL data).* The image segmentation pipeline was based on a previously published protocol<sup>13</sup>, with modifications as follows.

Main steps included (1) NoRMCorre correction of  $x$ - $y$  motion<sup>43</sup>; (2) trimming edges of video to remove pixels that entered or exited the FOV; (3) photobleach correction with  $b$ -spline fit; (4) penalized matrix decomposition (PMD) denoiser with parameters optimized on simulated data; (5) from each pixel, regress out residual motion artefacts using NoRMCorre-estimated motion trajectories; (6) manually crop blood vessels; (7) select areas of background to initialize background estimator; (8) superpixel-based demixing using non-negative matrix factorization (NMF) to calculate spatial footprints of cells and background; (9) regress the spatial footprint of cells out of the background (using a constant intercept term) to update spatial footprint of cells and background; and (10) apply the updated spatial and background footprints to calculate the temporal traces from the full denoised video.

Videos were first corrected for  $x$ - $y$  translational motion using the NoRMCorre algorithm<sup>43</sup>, and trimmed to the largest frame size that was in the FOV at all times. Each pixel of the video was then corrected for photobleaching by subtracting a  $b$ -spline fit of the pixel's fluorescence with knots 5,000 frames (5 s) apart. A PMD denoiser was then used to remove temporally uncorrelated noise from the video<sup>13</sup>. This method is a generalization of PCA: it divides the video into blocks and within each block decomposes the video into the sum of low-rank 'signal' and residual 'noise' that is uncorrelated pixel-to-pixel; this residual is then discarded.

Brain motion caused shifts of cells relative to the patterned illumination masks targeted to individual cells. Frame-by-frame translations corrected for brain motion, but introduced spurious apparent motion into the patterned illumination masks. This relative motion of cells and masks introduced spurious pixel-level motion artefacts, even in the motion-corrected videos. To reduce the effect of these artefacts, motion-correlated signals were projected out at the level of each pixel in the denoised video, using a general linear model. The regressors were the motion signals  $x$ ,  $y$ ,  $x^2$ ,  $y^2$  and  $xy$ , as computed by NoRMCorre. This procedure was performed independently in successive epochs of 5,000 frames (5 s). Regions of the video with visible blood flow were then manually masked to avoid high-frequency noise from passing blood cells.

Following a previously published study<sup>13</sup>, we defined 'superpixels' as collections of nearby pixels with correlated dynamics. We defined 'pure' superpixels using an iterative procedure that chose the sparsest temporal signals from the remaining superpixels and then projected out this signal from the other superpixels. These pure superpixels served as seeds to extract single-cell activity from the video. Regions without pure superpixels were manually selected as 'background' to seed the estimator of the background dynamics. A singular value decomposition on the background pixels yielded temporal and spatial components that initialized the background in the demixing analysis described below.

The videos were decomposed into temporal and spatial components through a local NMF on the denoised data; this NMF minimized the summed squared residual of the video after modelling both cell activity and a rank  $r$  background<sup>13</sup>. To enforce non-negativity, a pixel-wise minimum subtraction was first performed on the video. For the in vivo videos analysed, a rank-2 background model was used to capture different time-varying components of the background, while preserving cell signal. Higher-rank background models did not improve performance and sometimes spuriously assigned cell signals to background.

The spatial components,  $\mathbf{B}$ , of the background extracted from the NMF demixer typically contained contamination from cell footprints,  $\mathbf{A}$ . With a background of rank  $r$ ,  $n$  total cells in the FOV, and  $d$  pixels in a frame,  $\mathbf{B}$  represents the  $d \times r$  matrix of images of the background components and  $\mathbf{A}$  is a  $d \times n$  matrix of cell spatial footprints. To remedy this crosstalk, the spatial footprints of the cells were removed from the images of the background by a least-squares fit to create updated background spatial component  $\mathbf{B}^*$ . The use of  $\mathbf{B}^*$  facilitated the recovery of correlations between the cells and background lost in the demixer.

Finally, a least-squares estimate was used to regress the cell spatial footprints and updated background images on the full denoised and motion-corrected video to find the corresponding fluorescence traces for signal and background. No non-negativity constraints were imposed on these traces.

*Validation of the image-segmentation algorithm with simulated data.* We used numerical simulations to test and optimize the image segmentation code. First, we produced synthetic videos containing  $n$  partially overlapping 'cells' (disks) and a spatially heterogeneous time-varying background. We assigned a unique time-trace to each cell and to the background, as follows. We simulated  $n + 1$  independent waveforms using an Ornstein-Uhlenbeck process, a numerically simple model that captures the approximate statistics of neuronal subthreshold voltage dynamics<sup>45</sup>. We then used a Gram-Schmidt procedure to ensure that these waveforms were

precisely orthonormal. To challenge the image-segmentation algorithms with realistic correlated subthreshold signals, we then constructed correlated source waveforms, as follows. We selected a desired degree of subthreshold cross-correlation between the cells, and between each cell and the background. These correlations ranged from 0 (easy to segment) to 1 (impossible to segment). We used a Cholesky decomposition of the correlation matrix to compute the required linear combinations of orthonormal input functions. These  $n + 1$  linear combinations were assigned as the subthreshold fluctuations to the  $n$  cells and to the background.

We then assigned spikes to the cells with a mean spike rate of 8 Hz and Poisson-distributed interspike intervals. Finally, we added Poisson-distributed shot noise to each pixel at a level that approximately matched the noise level in our recordings. These simulations were designed to match the spatial and temporal correlation structure, and noise statistics, of real data as closely as possible—but with known ground-truth.

We then ran the videos through the image-segmentation algorithm and compared the extracted waveforms to the input waveforms. We quantified performance by calculating the cross-correlation of the extracted signals and the input signals. We sought algorithms that accurately extracted the input signals and that did not introduce spurious cell-cell or cell-background correlations. Extended Data Figure 6 shows that under realistic conditions the image-segmentation algorithm reliably captured the waveforms and correlational structure of the input.

*Validation of the image-segmentation algorithm with composite data.* To test the image-segmentation algorithm further, we challenged it with composite videos that consisted of real data. We took a series of videos in vivo of individual well-isolated cells either in focus or at 20- $\mu\text{m}$  defocus. We ran the image-segmentation algorithm on each video to extract the underlying single-cell waveforms. We then created composite videos by adding together pairs of independently recorded videos, translated such that around 50% of each cell overlapped with the other. In this way, mixed signals contributed substantially to the video, and the signal and noise properties were the same as in real data. These composite videos represented a worst-case scenario: in real data, we did not observe cells with such large overlap and such small focal offsets.

We ran the composite videos through the image-segmentation algorithm and compared the extracted waveforms to the waveforms extracted from the individual single-cell videos. Extended Data Figure 6 shows that the image-segmentation algorithm faithfully reproduced the input signals and their correlational structure. *Selection and scaling of fluorescence recordings.* Some morphologically distinct cells did not spike during the recording session, consistent with previous whole-cell patch-clamp recordings in the CA1<sup>16,17</sup> and were excluded from the analysis. Owing to cell-to-cell variations in steady-state background level, the offset of fluorescence traces was not judged to be meaningful. For presentation purposes, traces were scaled by their baseline noise, defined as the standard deviation after removal of the spikes and high-pass-filtering at 100 Hz (to remove slow oscillations). For presentation purposes, in the 'all-optical' data (Fig. 4 and Extended Data Fig. 10), we removed the blue-light photoactivation artefacts, as follows. We averaged the fluorescence traces from all cells to create a template function that characterized the photoartefact. We used a linear regression to scale this crosstalk function for each single cell and subtracted the estimated crosstalk. We also divided by the crosstalk function to correct for blue-light-dependent changes in voltage sensitivity. All analyses of spiking and subthreshold dynamics were performed on the raw data, without crosstalk correction. To ensure that the subthreshold power spectrum analysis (Fig. 4g, h and Extended Data Fig. 10b) was not biased by the blue-light photoactivation of paQuasAr3, we used only data from the 8-s steady illumination epochs and we normalized traces by the spike amplitude. This normalization enabled comparisons of subthreshold amplitudes between conditions (walking or quiet and with or without optogenetic stimulation) within a population of cells. Owing to systematic low-pass-filtering of the spike amplitudes by the reporter kinetics and camera exposure, we did not attempt to convert this normalization into an absolute millivolt scale.

*Spike detection, correlations and spike-triggered averaging.* A simple threshold-and-maximum procedure was applied for spike detection. Fluorescence traces were first high-pass-filtered and initial threshold was set at three times the noise level. This threshold was then manually adjusted if needed. All analyses of brain-state-dependent activity (Fig. 3) were performed on segments of the recordings comprising the last 9 s of the first rest period (quiet) and the first 9 s of the first walking period.

Fluorescence signals were first converted to  $\Delta F/F$ , in which  $F$  was the mean fluorescence in the epoch. The data were mean-subtracted in 1-s windows to correct for slow drifts in baseline fluorescence. To estimate the statistical errors in the cross-correlations, we calculated the cross-correlations between randomly selected cells from distinct FOVs. Spikes were not removed from the traces for calculations of auto- and cross-correlations.

STAs of the fluorescence (Fig. 3c, g and Extended Data Fig. 9) were calculated for each pair of simultaneously recorded cells, normalized to the range 0–1 and

then averaged across all cell pairs. Spike-triggered histograms of spike timing (Fig. 3d, h) were constructed for each spike with 10-ms bins. These histograms were then summed over all spikes and all cells and divided by the total number of spikes to yield a percentage of spikes in each time bin.

**Subthreshold power and power spectra.** To compare subthreshold powers (Fig. 2h) and power spectra (Figs. 2i, 4h) across conditions, signals were normalized by the optically recorded spike height. To determine whether changes in the power spectra were due to changes in spike rate or changes in subthreshold dynamics, we compared power spectra calculated from 'raw' traces with power spectra calculated from traces in which the spikes were digitally removed and replaced with smooth interpolations of the surrounding data. These two approaches yielded qualitatively similar power spectra, establishing that the bulk of the power in the traces was in the subthreshold components.

**Heating simulation.** To simulate optical tissue heating, we adapted a finite differencing model from a previously published study<sup>46</sup>, that was also previously further optimized<sup>47</sup>. This model accommodates heat conduction, metabolic heating and cooling by blood perfusion and by heat sinking from the objective, glass window and immersion water. We further modified the model for our imaging conditions: illumination of an  $r = 60\text{-}\mu\text{m}$  area, glass window attached to a metal cannula and 4-mm working distance objective. We used tabulated optical properties of brain tissue at 640 and 920 nm to compare heating effects from one-photon QuasAr imaging versus conventional two-photon microscopy.

**Reporting summary.** Further information on research design is available in the Nature Research Reporting Summary linked to this paper.

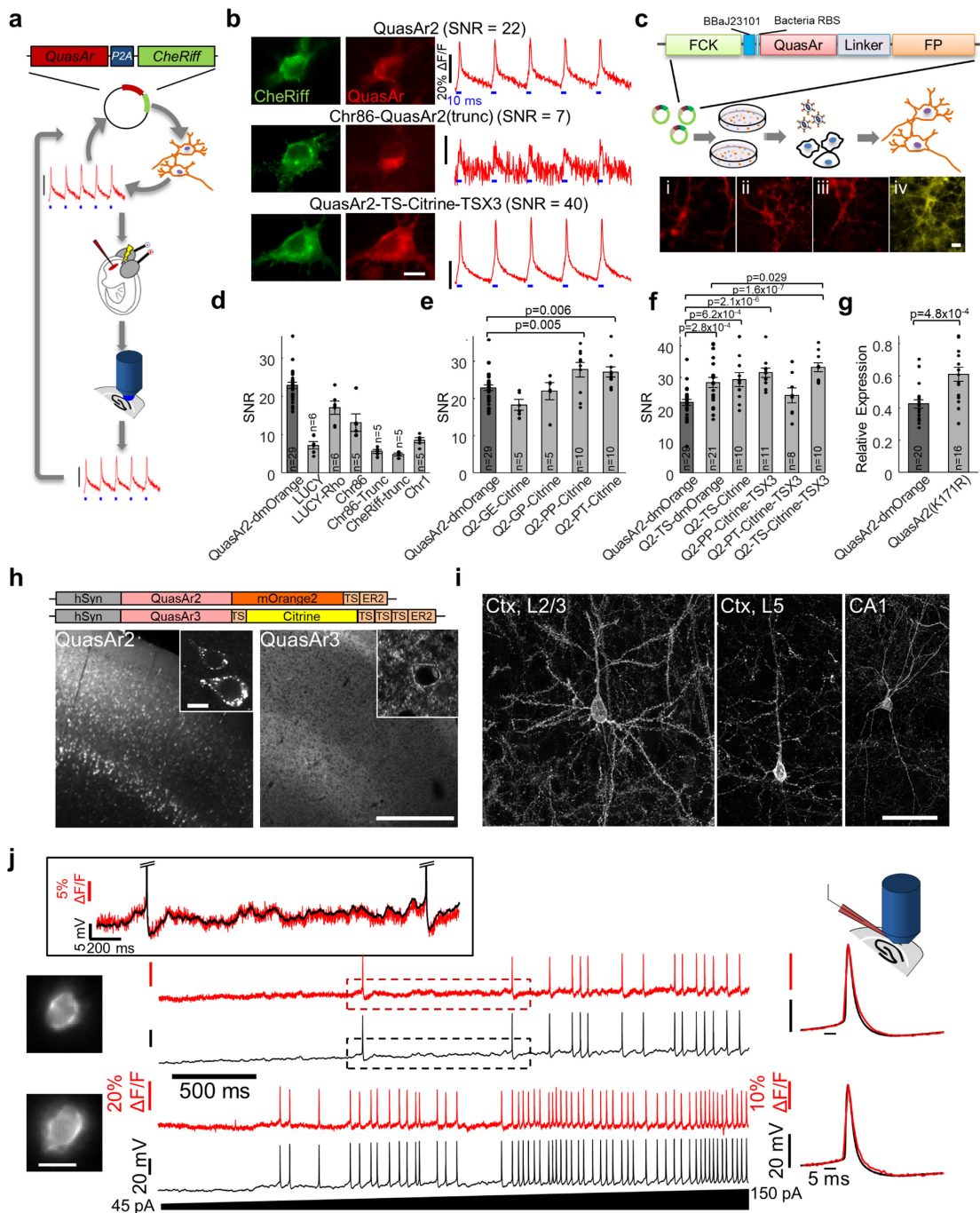
### Data availability

The datasets generated during the current study are available from the corresponding author upon reasonable request.

### Code availability

Custom data analysis codes are available from the corresponding author upon reasonable request.

29. Shaner, N. C. et al. Improving the photostability of bright monomeric orange and red fluorescent proteins. *Nat. Methods* **5**, 545–551 (2008).
30. Gradinaru, V. et al. Molecular and cellular approaches for diversifying and extending optogenetics. *Cell* **141**, 154–165 (2010).
31. Klapoetke, N. C. et al. Independent optical excitation of distinct neural populations. *Nat. Methods* **11**, 338–346 (2014).
32. Shepard, B. D., Natarajan, N., Protzko, R. J., Acres, O. W. & Pluznick, J. L. A cleavable N-terminal signal peptide promotes widespread olfactory receptor surface expression in HEK293T cells. *PLoS ONE* **8**, e68758 (2013).
33. Chow, B. Y. et al. High-performance genetically targetable optical neural silencing by light-driven proton pumps. *Nature* **463**, 98–102 (2010).
34. McIsaac, R. S. et al. Directed evolution of a far-red fluorescent rhodopsin. *Proc. Natl Acad. Sci. USA* **111**, 13034–13039 (2014).
35. Maclaurin, D., Venkatachalam, V., Lee, H. & Cohen, A. E. Mechanism of voltage-sensitive fluorescence in a microbial rhodopsin. *Proc. Natl Acad. Sci. USA* **110**, 5939–5944 (2013).
36. Daigle, T. L. et al. A suite of transgenic driver and reporter mouse lines with enhanced brain-cell-type targeting and functionality. *Cell* **174**, 465–480 (2018).
37. Molyneaux, B. J., Arlotta, P., Hirata, T., Hibi, M. & Macklis, J. D. Fezl1 is required for the birth and specification of corticospinal motor neurons. *Neuron* **47**, 817–831 (2005).
38. Krashes, M. J. et al. Rapid, reversible activation of AgRP neurons drives feeding behavior in mice. *J. Clin. Invest.* **121**, 1424–1428 (2011).
39. Adam, Y. & Mizrahi, A. Long-term imaging reveals dynamic changes in the neuronal composition of the glomerular layer. *J. Neurosci.* **31**, 7967–7973 (2011).
40. Dombeck, D. A., Harvey, C. D., Tian, L., Looger, L. L. & Tank, D. W. Functional imaging of hippocampal place cells at cellular resolution during virtual navigation. *Nat. Neurosci.* **13**, 1433–1440 (2010).
41. Goldey, G. J. et al. Removable cranial windows for long-term imaging in awake mice. *Nat. Protoc.* **9**, 2515–2538 (2014).
42. Kralj, J. M., Douglass, A. D., Hochbaum, D. R., Maclaurin, D. & Cohen, A. E. Optical recording of action potentials in mammalian neurons using a microbial rhodopsin. *Nat. Methods* **9**, 90–95 (2012).
43. Pnevmatikakis, E. A. & Giovannucci, A. NoRMCorre: an online algorithm for piecewise rigid motion correction of calcium imaging data. *J. Neurosci. Methods* **291**, 83–94 (2017).
44. Mukamel, E. A., Nimmerjahn, A. & Schnitzer, M. J. Automated analysis of cellular signals from large-scale calcium imaging data. *Neuron* **63**, 747–760 (2009).
45. Ricciardi, L. M. & Sacerdote, L. The Ornstein–Uhlenbeck process as a model for neuronal activity. I. Mean and variance of the firing time. *Biol. Cybern.* **35**, 1–9 (1979).
46. Stujenske, J. M., Spellman, T. & Gordon, J. A. Modeling the spatiotemporal dynamics of light and heat propagation for in vivo optogenetics. *Cell Rep.* **12**, 525–534 (2015).
47. Podgorski, K. & Ranganathan, G. Brain heating induced by near-infrared lasers during multiphoton microscopy. *J. Neurophysiol.* **116**, 1012–1023 (2016).



Extended Data Fig. 1 | See next page for caption.

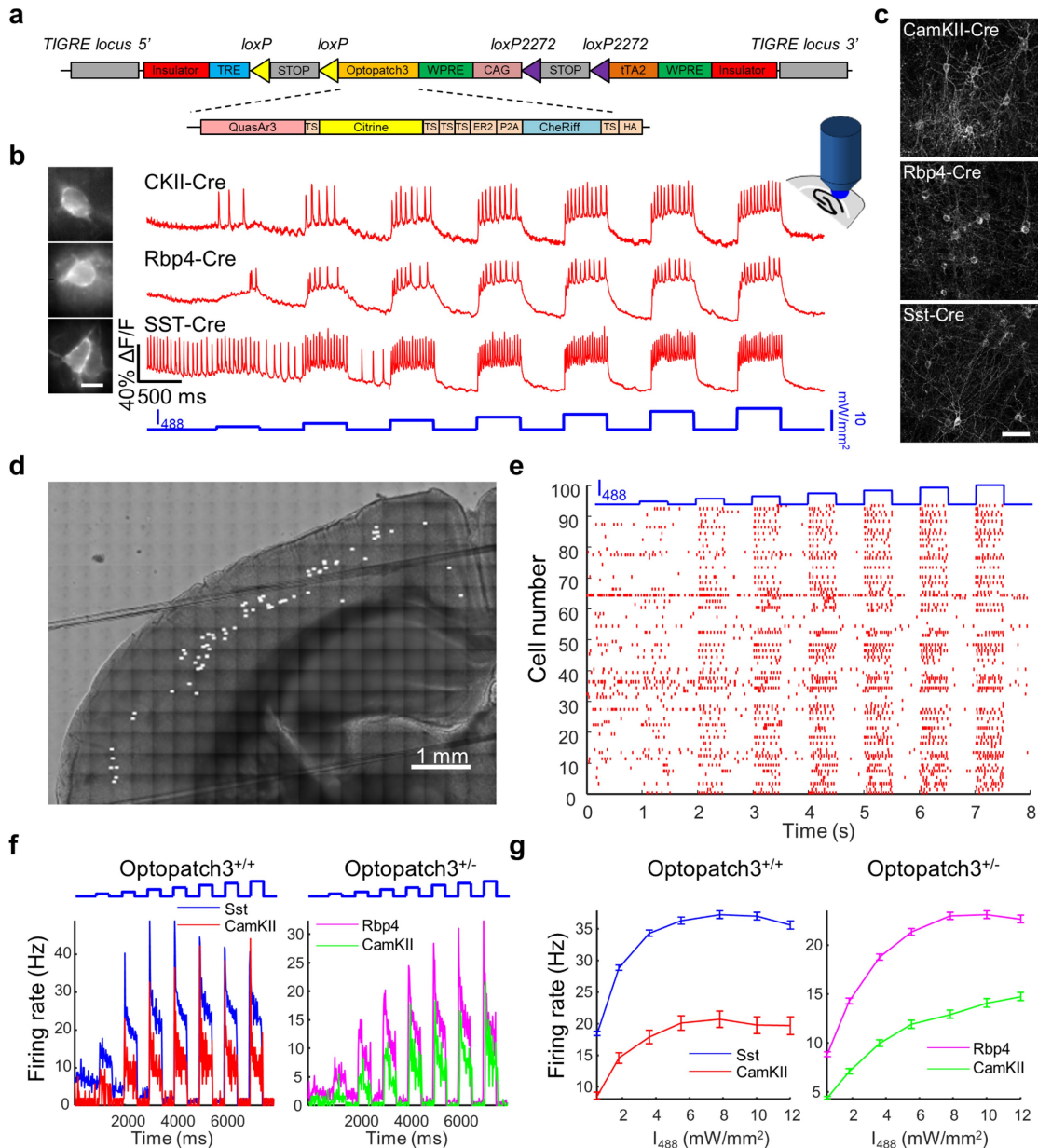
**Extended Data Fig. 1 | Development and characterization of QuasAr3.**

**a**, Screening pipeline. Rationally designed constructs were cloned in the Optopatch configuration, expressed in primary neurons and tested for spike SNR using light-induced spikes. Constructs with improved SNR were then expressed in vivo using in utero electroporation and tested for spike SNR in acute slices. The process was repeated iteratively. **b**, Examples of SNR measurements in cultured neurons. Left, wide-field epifluorescence images of GFP (green) fused to CheRiff, an opsin with excellent membrane trafficking. Middle, fluorescence of QuasAr (red) mutants. Scale bar, 10  $\mu\text{m}$ . Right, QuasAr fluorescence transients in response to optogenetically induced spikes (10 ms blue-light stimulation at 1 mW  $\text{mm}^{-2}$ ). Each construct was tested on at least five cultured neurons. **c**, Hierarchical screen for improved membrane trafficking of QuasAr variants (see Methods for details). Diagram, schematic of the FCK\_DuEx1.0 construct and overview of the screening pipeline. *E. coli* colonies were transformed with libraries in FCK\_DuEx1.0. The colonies with the brightest fluorescence were picked for lentivirus production and secondary screening in primary neuronal culture. Images, example images of the fluorescent protein (FP) channel of QuasAr2–FP fusions: (i) mOrange; (ii) mRuby2; (iii) mKate2; (iv) citrine. Scale bar, 10  $\mu\text{m}$ . **d**, SNR of N-terminal modifications compared with QuasAr2.

All constructs showed reduced SNR (see Methods for details).

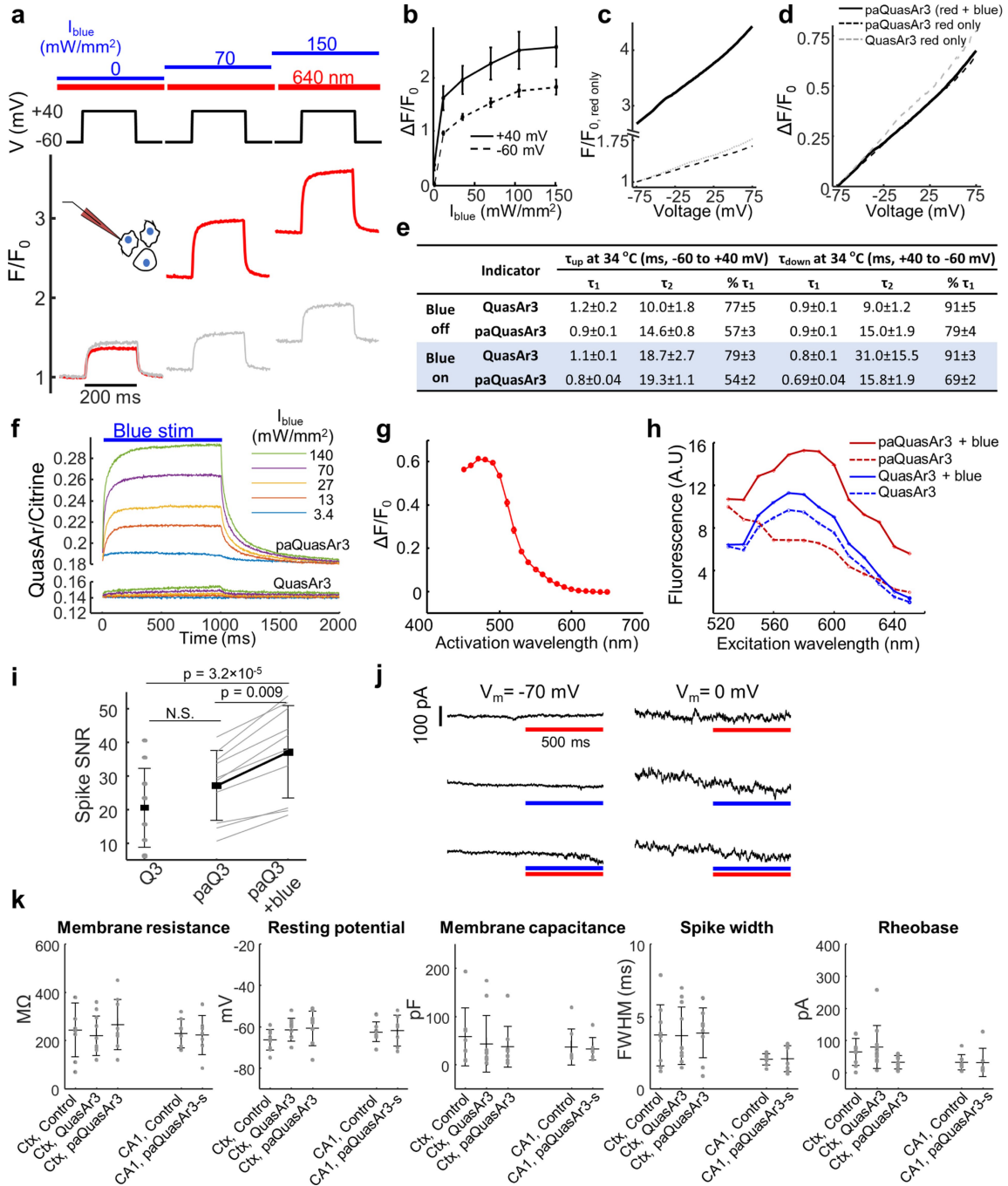
**e**, Replacing mOrange2 with Citrine as a fusion protein improved the trafficking only with two specific linkers. **f**, Adding additional TS sequences at the linker and C-terminal improved the spike SNR. **g**, The mutation K171R increased the expression level of QuasAr, quantified by normalizing QuasAr fluorescence by the fluorescence of the co-expressed CheRiff–GFP. **d–g**, Data are mean  $\pm$  s.e.m., one-tailed Student's *t*-test.

**h**, Top, diagram of the QuasAr2 and QuasAr3 constructs. Bottom, confocal images of brain slices expressing QuasAr2 and QuasAr3. Scale bar, 500  $\mu\text{m}$ . Insets, single-cell bodies; scale bar, 10  $\mu\text{m}$ . Representative images from  $n = 2$  mice (QuasAr2) and  $n = 3$  mice (QuasAr3). **i**, Confocal images of brain slices expressing Cre-dependent QuasAr3 with sparsity controlled by co-expression of hSyn-Cre. Scale bar, 50  $\mu\text{m}$ . **j**, Simultaneous fluorescence and patch-clamp recordings from two neurons expressing QuasAr3 using AAV virus in acute brain slices. Left, image of QuasAr3 fluorescence in the soma. Scale bar, 10  $\mu\text{m}$ . Middle, spiking during ramp current injection. Right, mean spike, overlay of fluorescence and voltage. Inset, boxed regions showing correspondence of optical and electrical recordings of subthreshold voltage overlaid. See Extended Data Fig. 3 for statistics.



**Extended Data Fig. 2 | Mapping neuronal excitability in Cre-on Optopatch3 transgenic mice (line Ai155).** **a**, Construct design for a Cre-dependent Optopatch3 transgenic mouse. **b**, Representative traces for all optical electrophysiology recordings in acute brain slices from Optopatch3 transgenic mice crossed with different Cre driver lines. Scale bar, 10  $\mu\text{m}$ . **c**, Confocal images showing citrine fluorescence from QuasAr3-citrine, in offspring of crosses between Optopatch3 mice and different Cre driver mice. Acute brain slices were prepared from mice aged 14 to 17 days and imaged in the cortex. Scale bar, 50  $\mu\text{m}$ . **d**, Composite bright-field image of a coronal brain slice from an *Rbp4-cre<sup>+/-</sup>;Optopatch3<sup>+/-</sup>* transgenic mouse, with locations of optical recordings marked with white spots. **e**, Spike raster showing 94 cells recorded sequentially from a single *Rbp4-cre<sup>+/-</sup>;Optopatch3<sup>+/-</sup>* acute brain slice. **f**, Optogenetic stimulus intensity-dependent firing rates in acute slices with different Cre drivers.

Left, slices that are homozygous for Optopatch3. Right, slices that are heterozygous for Optopatch3. **g**, Mean firing rate ( $F$ ), during a 500-ms stimulus as a function of stimulus intensity ( $I$ ) calculated from the data shown in **f**. Data are shown as mean  $\pm$  s.e.m. In the mice with Optopatch3 expression driven by CamKII-Cre, the  $F$ - $I$  curve for the *Optopatch3<sup>+/+</sup>* mice is compressed along the  $x$  axis relative to the *Optopatch3<sup>+/-</sup>* mice, which indicates a stronger optogenetic drive for a given optical stimulation strength in the mice homozygous for CheRiff. The decrease in firing rate at a strong stimulus in these mice is a signature of depolarization block. Data are from 128 cells from 5 slices from 2 *Sst-cre<sup>+/-</sup>;Optopatch3<sup>+/-</sup>* mice; 25 cells from 1 slice from 1 *CamKII-cre<sup>+/-</sup>;Optopatch3<sup>+/-</sup>* mouse; 152 cells from 6 slices from 4 *Rbp4-cre<sup>+/-</sup>;Optopatch3<sup>+/-</sup>* mice; 89 cells from 2 slices from 2 mice for *CamKII-cre<sup>+/-</sup>;Optopatch3<sup>+/-</sup>* mice.

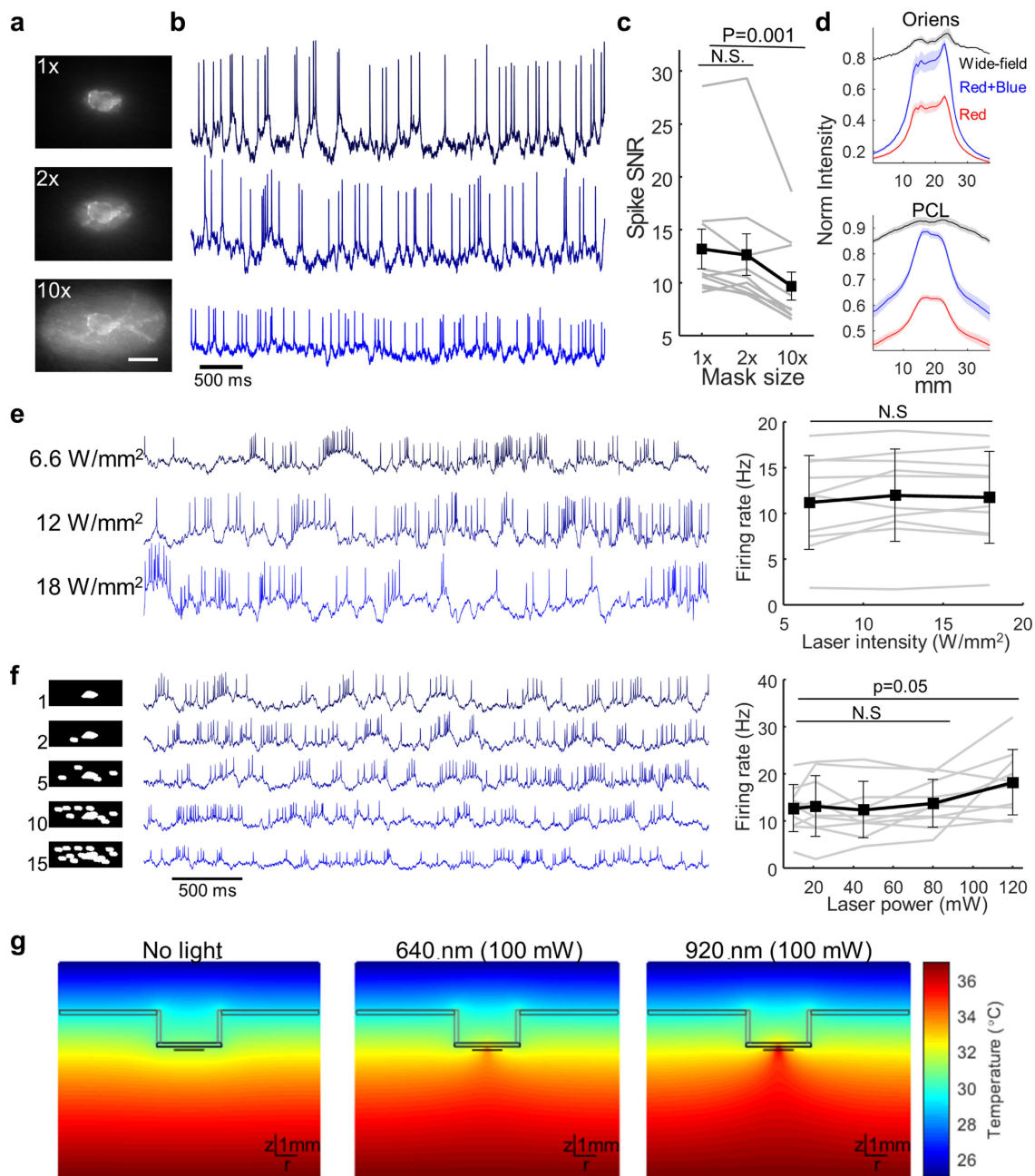


Extended Data Fig. 3 | See next page for caption.

**Extended Data Fig. 3 | Photophysical properties, kinetics and electrical properties of paQuasAr3.**

**a**, Photoactivation by blue light. Red lines, fluorescence of HEK293T cells that express paQuasAr3 during voltage steps under constant red illumination ( $10 \text{ W mm}^{-2}$ ) and variable blue illumination (average of  $n = 8$  cells). Grey lines, same experiment in HEK293T cells that express QuasAr3 (average of  $n = 7$  cells). **b**, PaQuasAr3 fluorescence compared to blue-light intensity at two membrane voltages ( $n = 8$  cells, mean  $\pm$  s.e.m.). Photoactivation showed saturation behaviour, with 50% maximum enhancement at  $I_{488 \text{ nm}} = 27 \text{ mW mm}^{-2}$ . **c**, Voltage-dependent near-infrared fluorescence of paQuasAr3 and QuasAr3 with and without blue light ( $150 \text{ mW mm}^{-2}$ ). All fluorescence values are normalized to fluorescence with red-only illumination at  $V_m = -75 \text{ mV}$ . **d**, Same data as c but each fluorescence trace was normalized to its value  $F_0$  at  $V_m = -75 \text{ mV}$ . Blue illumination enhanced the absolute fluorescence and the absolute voltage sensitivity, but the fractional voltage sensitivity ( $\Delta F/F_0$ ) was the same between QuasAr3 and paQuasAr3 and was not affected by blue illumination ( $n = 7$  cells in each condition,  $P = 0.91$ , one-way analysis of variance). **e**, Kinetics of QuasAr3 and paQuasAr3 measured in HEK293T cells. Cells were subjected to a square wave from  $-60 \text{ mV}$  to  $+40 \text{ mV}$  at  $5 \text{ Hz}$  (see **a**). Response transients were fitted to a double exponential. QuasAr3,  $n = 5$  cells; paQuasAr3,  $n = 9$  cells. Data are mean  $\pm$  s.e.m. Red intensity,  $10 \text{ W mm}^{-2}$ ; blue intensity,  $150 \text{ mW mm}^{-2}$ . **f**, Response of paQuasAr3 and QuasAr3 to steps of blue illumination. The blue-light enhancement arose with a  $50 \pm 14$ -ms time constant and subsided with a  $167 \pm 26$ -ms time

constant (mean  $\pm$  s.d.). Blue light activated paQuasAr3 was approximately twofold brighter than QuasAr3 (mean of  $n = 10$  cells). **g**, Action spectrum for photosensitization, measured in *E. coli* expressing paQuasAr3. Fluorescence was excited at  $\lambda_{\text{exc}} = 640 \text{ nm}$  and emission was collected from  $\lambda_{\text{em}} = 660\text{--}740 \text{ nm}$ . The activation wavelength was scanned from  $\lambda_{\text{act}} = 450\text{--}650 \text{ nm}$ . Peak activation was at  $\lambda_{\text{act}} = 470 \text{ nm}$ . **h**, Fluorescence excitation spectra with and without blue sensitization ( $40 \text{ mW mm}^{-2}$ ). The sensitized state of paQuasAr3 had a fluorescence excitation spectrum similar to QuasAr3, with peak excitation at  $\lambda_{\text{exc}} = 580 \text{ nm}$ . **i**, SNR of single spikes in acute slices for QuasAr3 ( $n = 10$  cells) and paQuasAr3 ( $n = 10$  cells) with either red light only or red and blue illumination (mean  $\pm$  s.d. paQuasAr3 with and without blue light, paired Student's *t*-test, paQuasAr3 red and blue illumination versus QuasAr3 red light only, Student's *t*-test). **j**, Voltage-clamp recordings in CA1 pyramidal cell expressing paQuasAr3-s showed no photocurrents in response to illumination with red light ( $640 \text{ nm}$ ,  $12 \text{ W mm}^{-2}$ ), blue light ( $488 \text{ nm}$ ,  $90 \text{ mW mm}^{-2}$ ) or a combination of the two lights, both when the cell was held at  $-70 \text{ mV}$  and at  $0 \text{ mV}$  (repeated in  $n = 2$  cells). **k**, Electrical properties measured by patch clamp in acute slices. QuasAr3 ( $n = 11$  cells, 6 slices, 2 mice) and paQuasAr3 ( $n = 9$  cells, 6 slices, 3 mice) were expressed in the visual cortex and compared with non-expressing cortical cells ( $n = 9$  cells, 7 slices, 7 mice). paQuasAr3-s ( $n = 7$  cells, 7 slices, 5 mice) was expressed in the CA1 pyramidal cell layer, and compared with non-expressing cells in that layer ( $n = 8$  cells, 6 slices, 5 mice). Data are mean  $\pm$  s.d.

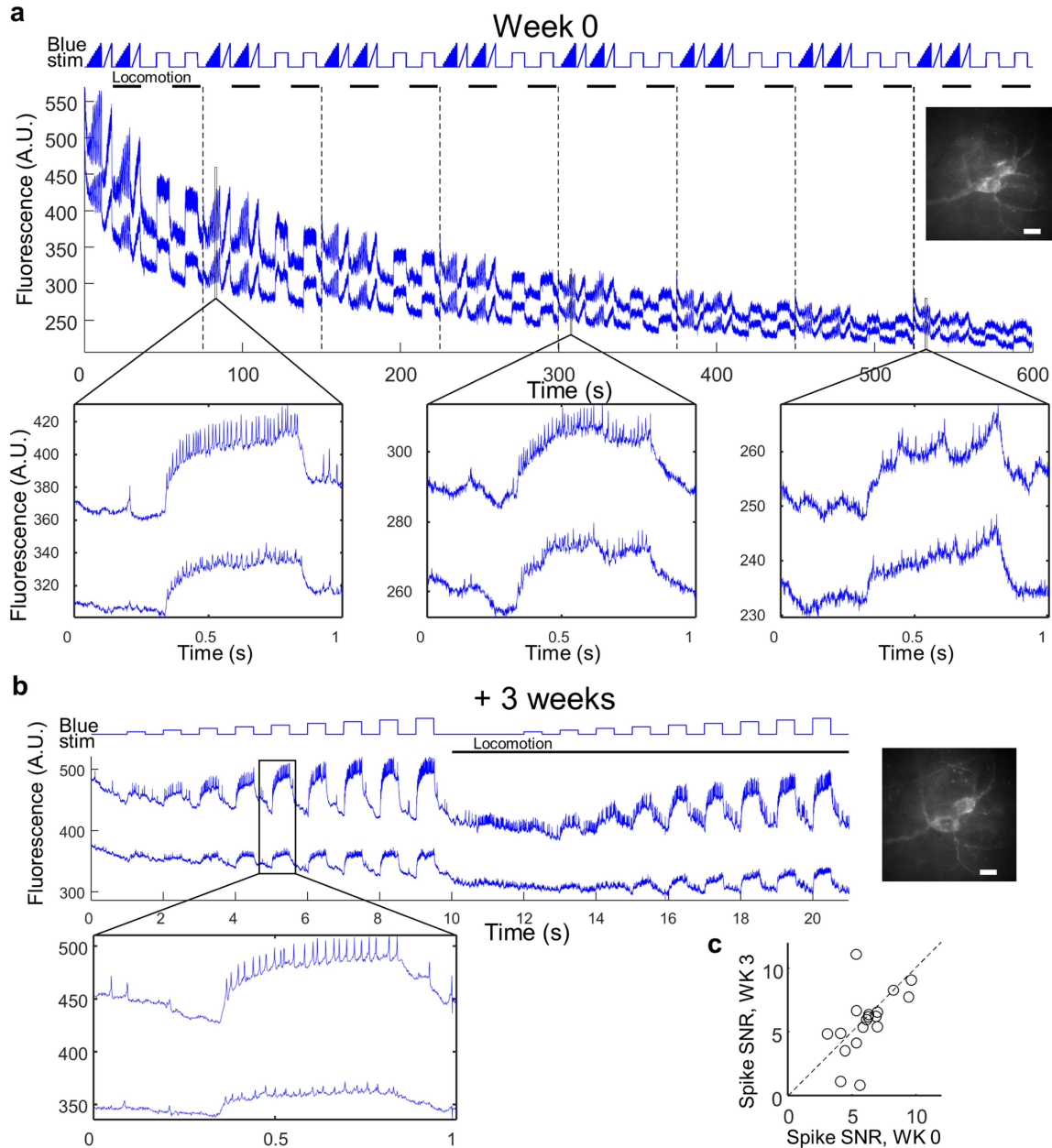


Extended Data Fig. 4 | See next page for caption.

**Extended Data Fig. 4 | Patterned illumination improves brain imaging and minimizes brain heating.**

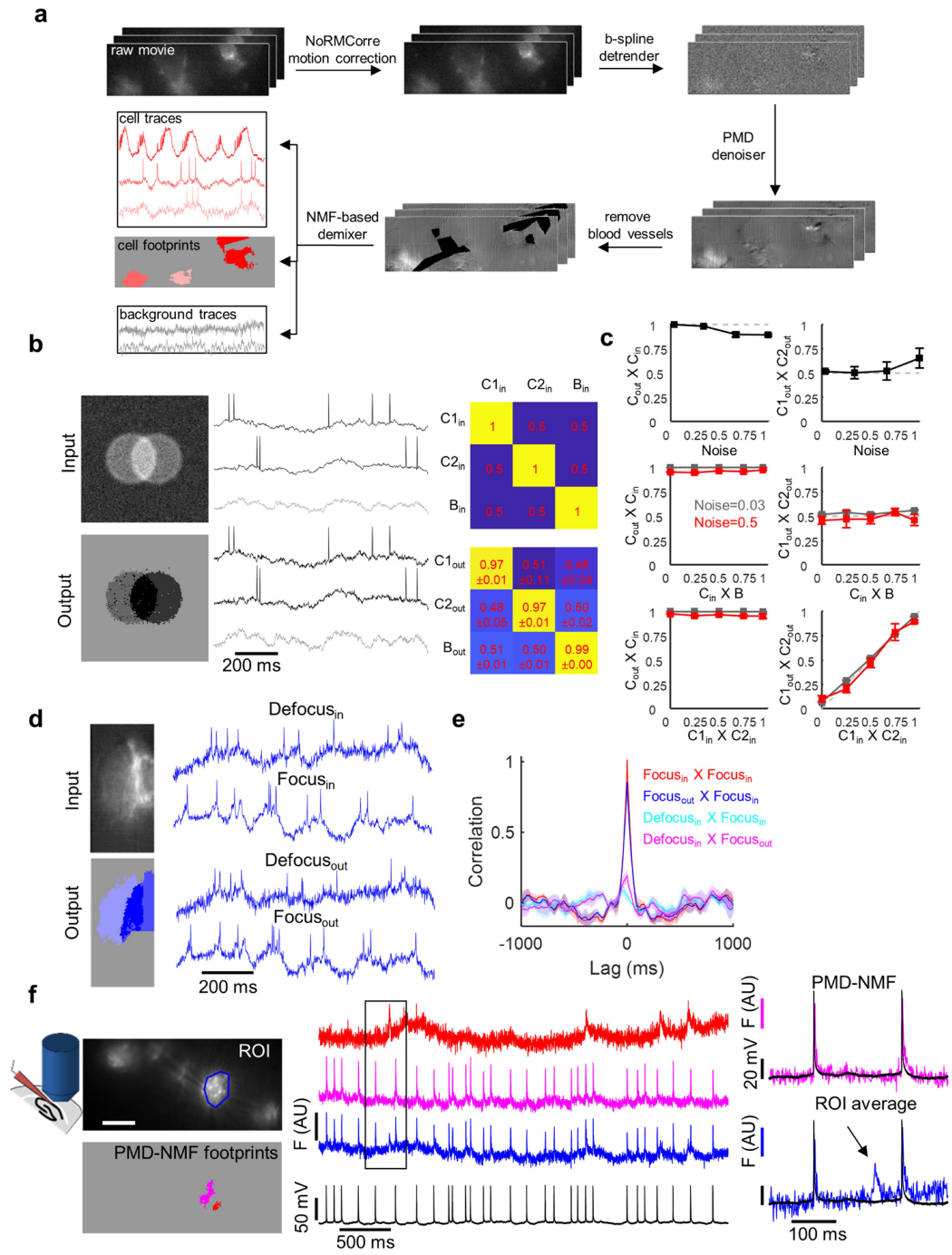
**a**, A single oriens interneuron was illuminated with red and blue light projected precisely onto the cell ( $1\times$ ) or with an oval mask of which the area was either twice ( $2\times$ ) or 10 times bigger ( $10\times$ ) than the cell. Scale bar,  $20\ \mu\text{m}$ . Illumination intensity was held constant across measurements. **b**, Spontaneous spiking activity of the oriens interneuron from **a** in an awake resting mouse. **c**, Mean spike SNR was similar with the  $2\times$  mask compared to the  $1\times$  mask ( $P = 0.2$ , two-sided paired Student's *t*-test) and significantly reduced with the  $10\times$  mask ( $P = 0.001$ , two-sided paired Student's *t*-test,  $n = 10$  cells from  $n = 2$  mice, data are mean  $\pm$  s.e.m.). **d**, Cross-section of near-infrared fluorescence of oriens or PCL cells imaged in anaesthetized mice and illuminated with either wide-field red illumination, patterned red illumination or patterned red and patterned blue illumination. The lower SBR in the PCL is attributed to the greater density of expressing cells. All cells visible in the focal plane were targeted with illumination, leading to higher background in the PCL. In the oriens, blue illumination increased the signal but not background. In the PCL, blue illumination modestly increased background, a consequence of light scattering between neighbouring cells. SBR values were as follows. PCL: wide field,  $0.27 \pm 0.02$ ; red only,  $0.95 \pm 0.063$ ; red and blue,  $1.31 \pm 0.08$ ;  $n = 64$  cells. Oriens: wide field,  $0.27 \pm 0.05$ ; red only,  $2.9 \pm 0.19$ ; red and blue,  $4.5 \pm 0.27$ ;  $n = 7$  cells.

Data are mean  $\pm$  s.e.m. (shown as line and shading). These data were used to calculate the improvement in SBR in Fig. 2d. **e**, Left, spontaneous activity of a representative oriens neuron in an awake, resting mouse illuminated with the indicated laser intensity. Right, population average shows no change in the firing rate in the illumination range tested (corresponding to 12.5–34 mW into the tissue,  $n = 10$  cells from 2 mice, data are mean  $\pm$  s.d.,  $P = 0.22$ , two-sided paired Student's *t*-test, N.S., not significant). **f**, FOVs with single oriens interneurons were imaged while illuminating with increasing number of masks around the cell to simulate the multicellular imaging conditions used in the PCL. Left, typical illumination pattern with the indicated number of masks. Middle, representative traces from an oriens FOV imaged in an awake, resting mouse with the indicated number of masks. Right, mean spontaneous firing rate as a function of the total laser power. Firing rates were stable with illumination of up to 10 masks (80 mW). Projection of 15 masks (120 mW) caused a modest increase in the spontaneous firing rates ( $n = 10$  cells from 2 mice, data are mean  $\pm$  s.d.,  $P = 0.05$ , two-sided paired Student's *t*-test). Subsequent experiments were restricted to ten or fewer masks. **g**, Simulated spatial temperature profile in brain tissue with an imaging cannula and immersion water. Profiles are shown for no illumination, 100-mW 640-nm illumination and 100-mW 920-nm illumination, corresponding to a two-photon imaging experiment.



**Extended Data Fig. 5 | Photostability of paQuasAr3-s in vivo during 'all-optical' excitability measurements.** **a**, Fluorescence in the mouse hippocampus was recorded for 10 min in total. Oriens SST cells expressed paQuasAr3-s and CheRiff-s and were illuminated with red light at  $12 \text{ W mm}^{-2}$  and stimulated with blue light (up to  $10 \text{ mW mm}^{-2}$ ) using the stimulation protocol presented at the top, during quiet and walking periods. The trace shows the fluorescence from two user-defined regions of interest after subtraction of the background from a cell-free region. The baseline signal photobleached in both cells by around 50% during

this interval. Top, total acquisition. Dashed lines denote separate videos. Bottom, magnified views of the indicated regions from the top graph. Similar recordings were performed in five FOVs. **b**, The same two cells were imaged three weeks later. While at the end of the initial 10-min recording the SNR was low due to photobleaching, 3 weeks later the signal had recovered. Images show wide-field epifluorescence images of the cells in the two imaging sessions. Scale bars,  $20 \mu\text{m}$ . **c**, Spike SNR was on average stable in repeated recordings over three weeks ( $P = 0.34$ , two-sided paired Student's  $t$ -test).

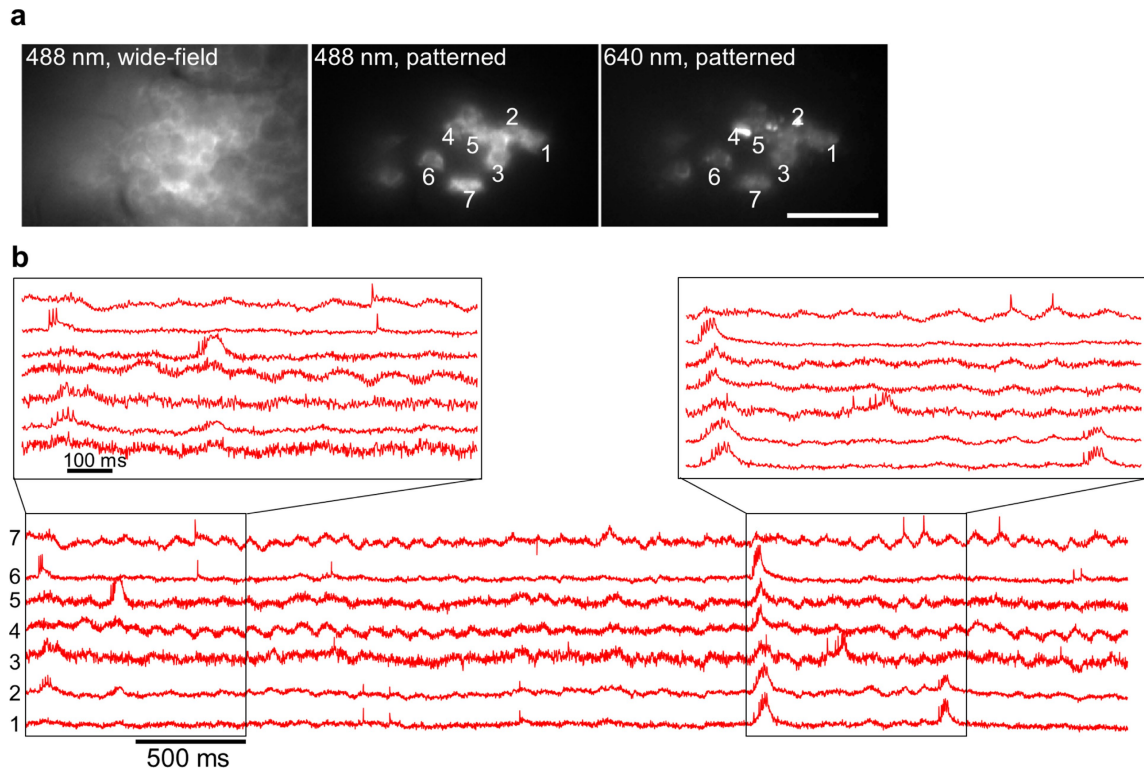


Extended Data Fig. 6 | See next page for caption.

**Extended Data Fig. 6 | Validation of the pipeline for signal extraction from dense PCL videos using PMD–NMF.**

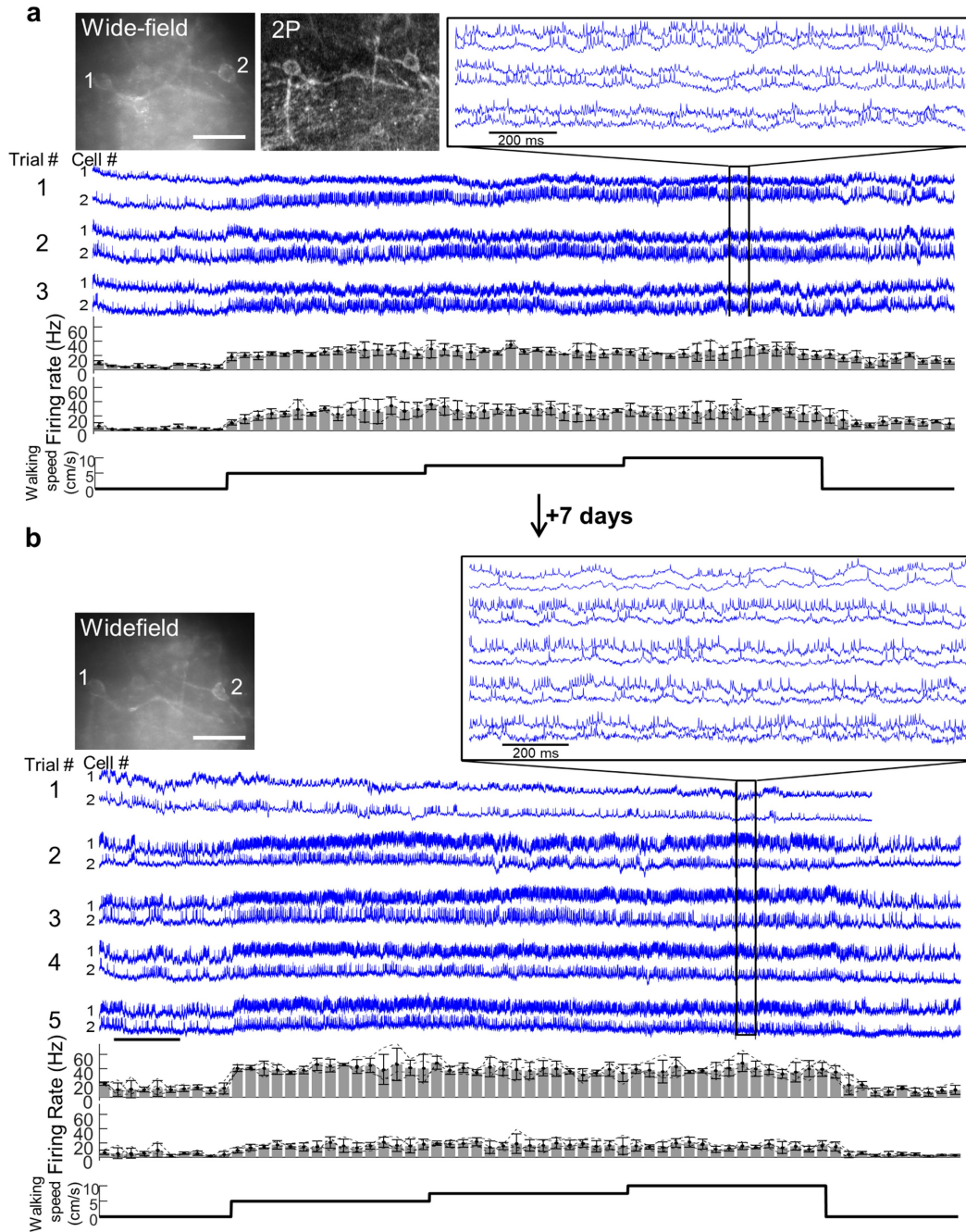
**a**, Illustration of the segmentation pipeline: raw videos were first corrected for motion, followed by photobleaching correction, PMD denoising, manual removal of blood vessels and demixing using NMF. The pipeline produced waveforms that correspond to individual cell traces and to the background (see Methods for details). **b**, Testing the pipeline using simulated data composed of two cells partially overlapping in space, and with varying levels of correlation in their subthreshold voltages and with the background. Poisson-distributed shot noise was added to each pixel to mimic experimental noise. Left, image of the input video pixel-wise s.d. and the output cell footprints. Middle, input waveforms and the pipeline output waveforms. Top right, correlation matrix of input signals (C1, C2, cells 1 and 2; B, background). Bottom right, cross-correlation of output waveforms with input waveforms, data are mean  $\pm$  s.d. for  $n = 5$  simulations. **c**, Performance of the pipeline as a function of input parameters ( $n = 5$  simulations per condition). Top, output-to-input correlation and output C1-to-C2 cross-correlation as a function of the pixel noise level. Noise is scaled to the spike amplitude, input C1-to-C2 cross-correlation is 0.5 and the input correlation with the background is also 0.5. Middle, output-to-input correlation and output C1-to-C2 cross-correlation as a function of the correlation between the input and the background, at two noise levels. Input C1-to-C2 correlation is 0.5. Bottom, output-to-input correlation and output C1-to-C2 cross-correlation as a function of the cross-correlation between input C1 and C2 at two noise

levels. Input correlation with background is 0.5. (data are mean  $\pm$  s.e.m.). **d**, Testing the pipeline with composite videos composed from real data. We imaged FOVs with single oriens neurons spontaneously spiking in awake, resting mice. Each cell was imaged in the focal plane, and then at 20- $\mu$ m defocus. The two videos were first processed with the pipeline to extract the ground-truth input signals and then the videos were summed such that the focused and defocused cells were about 50% overlapping. We then ran the blended videos through the pipeline and compared outputs to the input traces using cross-correlation analysis. **e**, Mean cross-correlograms of five FOVs processed as described in **d**, showing that the segmentation pipeline accurately reproduced the correlational structure of the inputs even under these challenging conditions. Data are mean  $\pm$  s.e.m. (line and shading). **f**, Validation of the image segmentation pipeline using patch-clamp recording as the ground-truth. Top left, FOV with dense expression of paQuasAr3-s in CA1 PCL in an acute brain slice. The FOV was imaged while the voltage in the blue outlined cell was recorded by manual patch clamp. Bottom left, two of the spatial footprints identified by the PMD–NMF pipeline. Middle, ground-truth voltage recording (black), flat average region of interest around the cell (blue) and two PMD–NMF units (magenta and red). The flat average region of interest trace showed fluctuations that were not present in the patch-clamp recording, presumably from an out-of-focus cell. These events were absent in the magenta PMD–NMF demixed trace. Right, magnification of the indicated trace inset. Arrow indicates the out-of-focus event. This experiment was performed once.



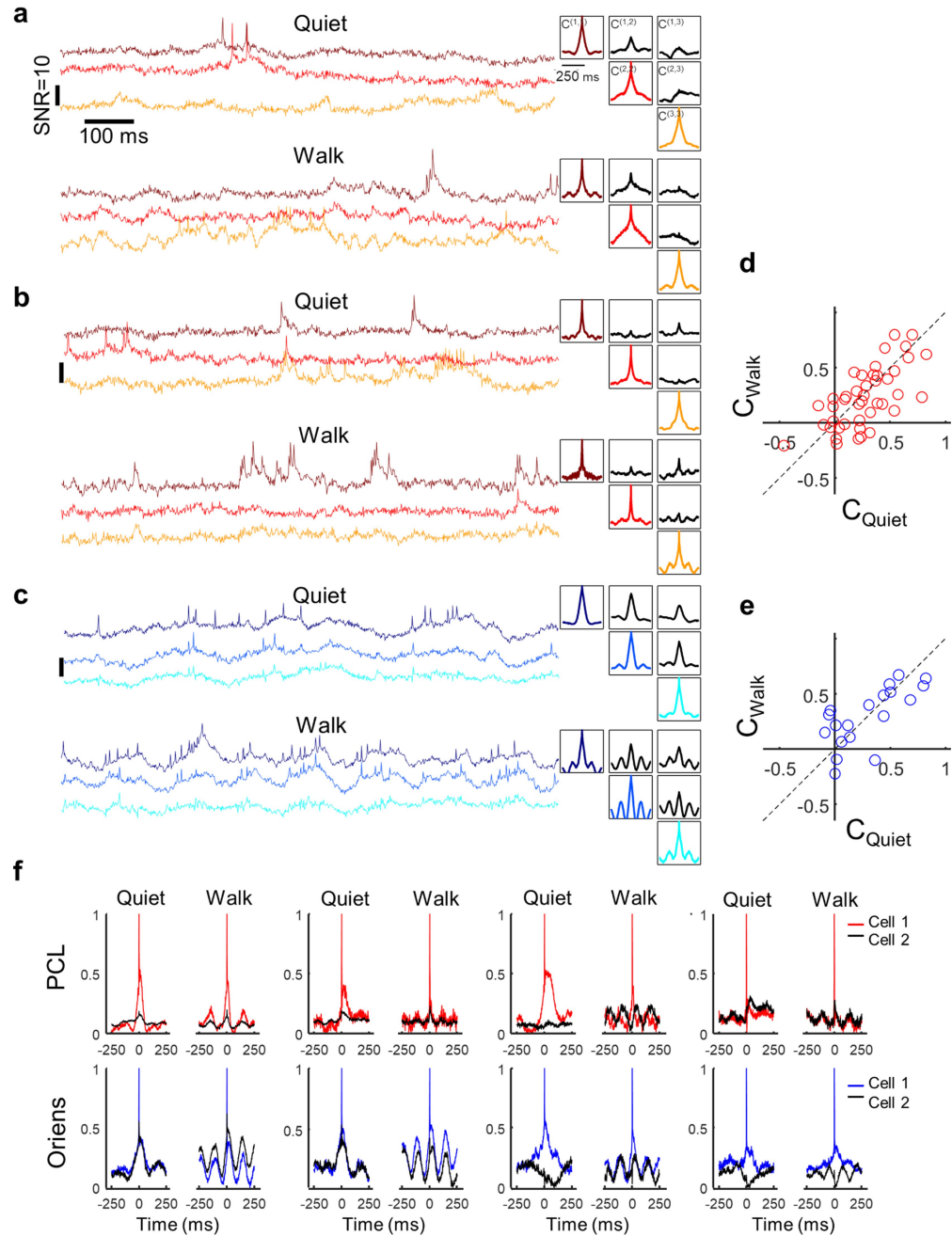
**Extended Data Fig. 7 | Simultaneous optical recording from seven spiking cells in the PCL of an anaesthetized mouse.** The mouse expressed paQuasAr3-s. **a**, Left, wide-field epifluorescence image of citrine fluorescence. Middle, same FOV with patterned blue illumination. Right, same FOV with patterned red illumination. Numbers indicate

individual cells. **b**, Simultaneous fluorescence recordings from seven cells. Magnifications show synchronized complex spikes and action potentials that occur on top of subthreshold oscillations. This experiment was performed once.



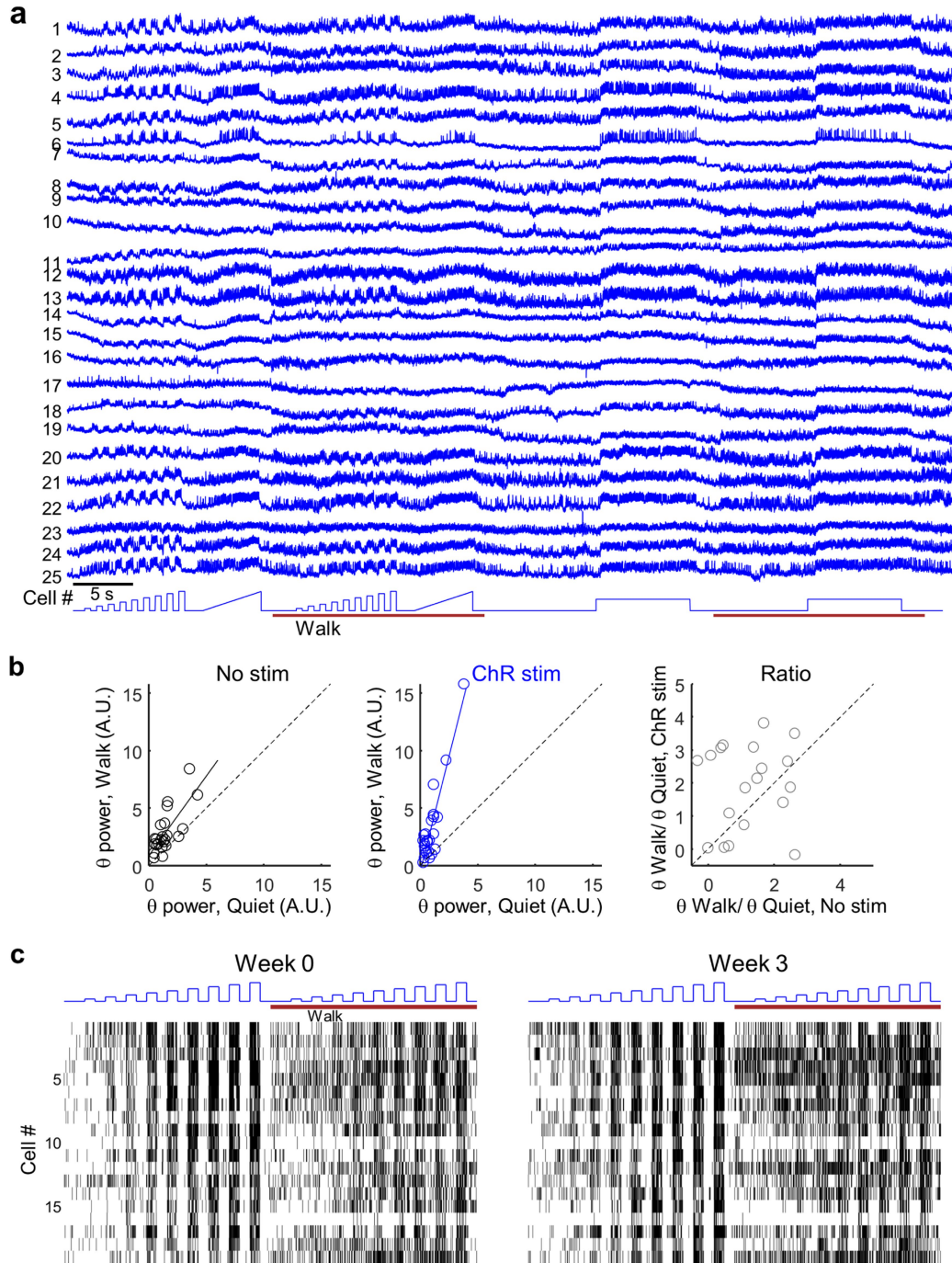
**Extended Data Fig. 8 | Chronic recordings of oriens neurons in hippocampus.** **a**, Top left, wide-field epifluorescence and two-photon images showing two oriens interneurons. Scale bar, 50  $\mu\text{m}$ . Middle, fluorescence recordings from the 2 cells during 3 consecutive repeats of a 65-s protocol. The protocol consisted of 10 s of rest, followed by 15-s epochs of walking at speeds of 5, 7.5 and 10  $\text{cm s}^{-1}$ , successively, followed

by 10 s of rest. Inset (top right) shows the optical traces with clearly resolved spikes and subthreshold events. Bottom, average spike rate across three trials of the two cells (data are mean  $\pm$  s.d.). **b**, Same two neurons and same protocol as in **a**, recorded seven days later. Trial 1 was only spontaneous activity without locomotion.



**Extended Data Fig. 9 | Examples of brain-state-dependent intercellular correlations and STAs for single pairs of cells.** a–c, Left, magnified sections of recordings from trios of cells in the PCL (a, b) and oriens (c). Top, recordings during quiet. Bottom, recordings from the same cells during walking. Right, auto- and cross-correlations of the fluorescence traces, calculated from the complete 9-s recording in each brain region and behavioural state. The auto- and cross-correlations clearly show enhanced

$\theta$ -rhythm in both brain regions during walking and differing cross-correlations between simultaneously recorded pairs of cells. d, e, Distribution of equal-time correlation coefficients between pairs of simultaneously recorded cells in the PCL (d) and oriens (e). f, Three examples of single-pair STA fluorescence during quiet (left) and walking (right) in the PCL (top) and oriens (bottom).



**Extended Data Fig. 10 | Optopatch measurements of hippocampal SST neurons. a,** Fluorescence waveforms of all 25 SST cells shown in Fig. 4. **b,** Cell-by-cell comparison of the change in  $\theta$ -band (6.7 to 8.3 Hz) power between walking and quiet brain states. Left, without optogenetic stimulation. Middle, same cells with tonic optogenetic stimulation. Right,

ratio of  $\theta$ -band enhancement (walking versus quiet) with optogenetic stimulation versus without (cell-by-cell comparison for the data in Fig. 4h). **c,** Spike raster of 19 SST cells imaged at week 0 and week 3 and stimulated with the blue light protocol at the top (full dataset for the data in Fig. 4j-k).

## Reporting Summary

Nature Research wishes to improve the reproducibility of the work that we publish. This form provides structure for consistency and transparency in reporting. For further information on Nature Research policies, see [Authors & Referees](#) and the [Editorial Policy Checklist](#).

### Statistics

For all statistical analyses, confirm that the following items are present in the figure legend, table legend, main text, or Methods section.

- |                                     |  |
|-------------------------------------|--|
| n/a                                 | Confirmed  |
| <input type="checkbox"/>            | <input checked="" type="checkbox"/> The exact sample size ( $n$ ) for each experimental group/condition, given as a discrete number and unit of measurement  |
| <input type="checkbox"/>            | <input checked="" type="checkbox"/> A statement on whether measurements were taken from distinct samples or whether the same sample was measured repeatedly  |
| <input type="checkbox"/>            | <input checked="" type="checkbox"/> The statistical test(s) used AND whether they are one- or two-sided<br><i>Only common tests should be described solely by name; describe more complex techniques in the Methods section.</i>   |
| <input type="checkbox"/>            | <input checked="" type="checkbox"/> A description of all covariates tested   |
| <input type="checkbox"/>            | <input checked="" type="checkbox"/> A description of any assumptions or corrections, such as tests of normality and adjustment for multiple comparisons  |
| <input type="checkbox"/>            | <input checked="" type="checkbox"/> A full description of the statistical parameters including central tendency (e.g. means) or other basic estimates (e.g. regression coefficient) AND variation (e.g. standard deviation) or associated estimates of uncertainty (e.g. confidence intervals) |
| <input type="checkbox"/>            | <input checked="" type="checkbox"/> For null hypothesis testing, the test statistic (e.g. $F$ , $t$ , $r$ ) with confidence intervals, effect sizes, degrees of freedom and $P$ value noted<br><i>Give <math>P</math> values as exact values whenever suitable.</i>                            |
| <input checked="" type="checkbox"/> | <input type="checkbox"/> For Bayesian analysis, information on the choice of priors and Markov chain Monte Carlo settings  |
| <input checked="" type="checkbox"/> | <input type="checkbox"/> For hierarchical and complex designs, identification of the appropriate level for tests and full reporting of outcomes  |
| <input checked="" type="checkbox"/> | <input type="checkbox"/> Estimates of effect sizes (e.g. Cohen's $d$ , Pearson's $r$ ), indicating how they were calculated  |

*Our web collection on [statistics for biologists](#) contains articles on many of the points above.*

### Software and code

Policy information about [availability of computer code](#)

Data collection

Data analysis

For manuscripts utilizing custom algorithms or software that are central to the research but not yet described in published literature, software must be made available to editors/reviewers. We strongly encourage code deposition in a community repository (e.g. GitHub). See the Nature Research [guidelines for submitting code & software](#) for further information.

### Data

Policy information about [availability of data](#)

All manuscripts must include a [data availability statement](#). This statement should provide the following information, where applicable:

- Accession codes, unique identifiers, or web links for publicly available datasets
- A list of figures that have associated raw data
- A description of any restrictions on data availability

### Field-specific reporting

Please select the one below that is the best fit for your research. If you are not sure, read the appropriate sections before making your selection.

- Life sciences       Behavioural & social sciences       Ecological, evolutionary & environmental sciences

## Life sciences study design

All studies must disclose on these points even when the disclosure is negative.

|                 |   |
|-----------------|---|
| Sample size     | Sample sizes were not predetermined and were based on similar reports in the literature. This is reported in the Methods.   |
| Data exclusions | Mice with aberrant optical implants were excluded from analyses. Voltage imaging data were analyzed only from cells that clearly showed spiking activity as described in the Methods. |
| Replication     | All experiments were repeated in multiple biological replicates as described. A detailed experimental protocol is provided to facilitate replication by others.                       |
| Randomization   | The experiments were not randomized   |
| Blinding        | The investigators were not blinded to the experimental condition.   |

## Reporting for specific materials, systems and methods

We require information from authors about some types of materials, experimental systems and methods used in many studies. Here, indicate whether each material, system or method listed is relevant to your study. If you are not sure if a list item applies to your research, read the appropriate section before selecting a response.

### Materials & experimental systems

| n/a                                 | Involved in the study   |
|-------------------------------------|---|
| <input checked="" type="checkbox"/> | <input type="checkbox"/> Antibodies                             |
| <input type="checkbox"/>            | <input checked="" type="checkbox"/> Eukaryotic cell lines       |
| <input checked="" type="checkbox"/> | <input type="checkbox"/> Palaeontology                          |
| <input type="checkbox"/>            | <input checked="" type="checkbox"/> Animals and other organisms |
| <input checked="" type="checkbox"/> | <input type="checkbox"/> Human research participants            |
| <input checked="" type="checkbox"/> | <input type="checkbox"/> Clinical data                          |

### Methods

| n/a                                 | Involved in the study                           |
|-------------------------------------|---|
| <input checked="" type="checkbox"/> | <input type="checkbox"/> ChIP-seq               |
| <input checked="" type="checkbox"/> | <input type="checkbox"/> Flow cytometry         |
| <input checked="" type="checkbox"/> | <input type="checkbox"/> MRI-based neuroimaging |

## Eukaryotic cell lines

Policy information about [cell lines](#)

|   |  |
|---|--|
| Cell line source(s)   | HEK293T cells (ATCC; CRL-11268)            |
| Authentication  | Cell lines were authenticated by ATCC      |
| Mycoplasma contamination  | Cells were tested negative for mycoplasma. |
| Commonly misidentified lines (See <a href="#">ICLAC</a> register) | N/A  |

## Animals and other organisms

Policy information about [studies involving animals](#); [ARRIVE guidelines](#) recommended for reporting animal research

|                         |  |
|-------------------------|--|
| Laboratory animals      | Species, strain, sex, and age are reported for each experiment in the Methods  |
| Wild animals            | N/A  |
| Field-collected samples | N/A  |
| Ethics oversight        | All procedures involving animals were in accordance with the National Institutes of Health Guide for the care and use of laboratory animals and were approved by the Harvard University Institutional Animal Care and Use Committee (IACUC). |

Note that full information on the approval of the study protocol must also be provided in the manuscript.